

An Experimental Setup for Heterogeneous Catalysis on Atomically Defined Metal Nanostructures

Présentée le 17 juin 2021

Faculté des sciences de base
Laboratoire de nanostructures superficielles
Programme doctoral en physique

pour l'obtention du grade de Docteur ès Sciences

par

Jean-Guillaume DE GROOT

Acceptée sur proposition du jury

Prof. F. Courbin, président du jury
Prof. H. Brune, Dr M. Pivetta, directeurs de thèse
Dr R. Schaub, rapporteur
Dr C. Wäckerlin, rapporteur
Prof. M. Grioni, rapporteur

Abstract

The main objective of this PhD thesis is to link the atomic scale structure to the catalytic properties of self-assembled nanostructures. The growth and characterization of these nanostructures was carried out in an ultra-high vacuum (UHV) chamber initially designed for the study of the kinetics of epitaxial growth of thin films and nanostructures by variable temperature scanning tunneling microscopy. During this PhD thesis, we built a very sensitive and selective gas detector based on a quadrupole mass spectrometer and adapted to the geometry of this UHV system. The proper functioning of the gas detector is confirmed by temperature programmed desorption measurements of Xe on Ag(100) which demonstrate the very high sensitivity of the device up to about 10^{-6} monolayer (ML). The zero-order desorption parameters obtained for the first monolayer of Xe adsorbed on Ag(100) are $E_d = 0.22 - 0.23$ eV with a prefactor ν_0 between $4 \times 10^{12} \text{ s}^{-1}$ and $1 \times 10^{13} \text{ s}^{-1}$.

An exchange process between Fe adatoms and Ag atoms from the Ag(100) surface is identified by means of temperature programmed desorption of N_2 . Desorption spectra suggest that the exchange is complete at an annealing temperature of 140 K.

Our study of the catalytic activity of metal nanostructures focuses on the ability of passivated Fe clusters to adsorb N_2 molecules without dissociating them, which is a fundamental step in the bio-inspired heterogeneous catalysis of ammonia. The first system investigated for the growth of Fe clusters is MgO/Ag(100). Diffusion of Fe adatoms deposited on a MgO monolayer is observed from an annealing temperature of 280 K onwards. Fe clusters with an average size of 12.1 ± 0.5 atoms are obtained on a MgO monolayer by thermal ripening of 0.072 ML of Fe deposited at 40 K. No sign of N_2 adsorption was observed on these clusters by thermal programmed desorption investigation.

The second system chosen for the growth of Fe clusters is graphene/Ir(111) obtained by chemical vapor deposition. The deposition of 0.3 and 0.4 ML of Fe on a graphene/Ir(111) sample at 50 K, followed by annealing at 300 K, results in a superlattice of Fe clusters which matches the periodicity of the moiré pattern formed by graphene/Ir(111). The expected mean cluster size is 26 atoms for 0.3 ML of Fe, and 35 atoms for 0.4 ML of Fe. The temperature stability of the clusters obtained with 0.4 ML Fe is investigated from 300 K to 600 K. It is established that Smoluchowski ripening takes place as the annealing temperature increases and the superlattice structure has completely disappeared after annealing at 600 K. Temperature programmed desorption of molecularly

Abstract

adsorbed N₂ at 50 K on a sample with 0.4 ML of Fe deposited on graphene/Ir(111) reveals three desorption peaks at 120 K, 92 K, and 60 K. In addition, slow dissociation of nitrogen molecules at 50 K adsorbed on the higher binding energy sites is demonstrated.

Keywords : heterogeneous catalysis, nanostructures, clusters, Fe, MgO, Ag(100), graphene, Ir(111), scanning tunneling microscope, temperature programmed desorption, quadrupole mass spectrometer.

Résumé

L'objectif principal de cette thèse de doctorat est de faire le lien entre la structure atomique et les propriétés catalytiques de nanostructures auto-assemblées. La croissance et la caractérisation de ces nanostructures ont été effectuées dans une chambre ultravide initialement conçue pour l'étude de la cinétique de croissance épitaxiale des couches minces et de nanostructures par microscopie à effet tunnel à température variable. Au cours de cette thèse de doctorat, nous avons construit un détecteur de gaz basé sur un spectromètre de masse quadripolaire et adapté à la géométrie de ce système ultravide. Le bon fonctionnement du détecteur de gaz est démontré par des désorptions programmées en température de Xe sur une surface de Ag(100) qui ont permis de vérifier la très haute sensibilité du dispositif qui est d'environ 10^{-6} monocouche (MC). Les paramètres de désorption d'ordre zéro obtenus pour la première monocouche de Xe adsorbé sur Ag(100) sont $E_d = 0.22 - 0.23$ eV avec un préfacteur ν_0 entre $4 \times 10^{12} \text{ s}^{-1}$ et $1 \times 10^{13} \text{ s}^{-1}$.

Un processus d'échange entre des atomes isolés de Fe et des atomes de Ag de la surface d'Ag(100) a été identifié au moyen de désorptions programmées en température de N₂. Les spectres de désorption suggèrent que l'échange est complet à partir d'une température de recuit de 140 K.

Notre étude de l'activité catalytique de nanostructures de métal se focalise sur la capacité pour des agrégats de Fe préalablement passivés d'adsorber des molécules de N₂ sans les dissocier, étape fondamentale dans le processus de catalyse hétérogène de l'ammoniac bio-inspiré. Le premier système étudié pour la croissance des agrégats de Fe est MgO sur Ag(100). La diffusion des atomes isolés de Fe déposés sur une monocouche de MgO est observée à partir d'une température de recuit d'au moins 280 K. Des agrégats de Fe avec une taille moyenne de 12.1 ± 0.5 atomes sont obtenus sur une monocouche de MgO par le mûrissement thermique de 0.072 MC de Fe préalablement déposé à 40 K. Aucun signe d'adsorption de N₂ n'a été observé sur ces agrégats.

Le second système choisi pour la croissance des agrégats de Fe est le graphène sur Ir(111) obtenu par dépôt chimique en phase vapeur. Le dépôt de 0.3 et 0.4 MC de Fe sur un échantillon de graphène/Ir(111) à 50 K, suivi d'un recuit à 300 K, engendre un super-réseau d'agrégats de Fe qui suit la périodicité du moiré formé par le graphène sur Ir(111). La taille moyenne théorique attendue des agrégats est 26 atomes pour 0.3 MC de Fe, et 35 atomes pour 0.4 MC de Fe. La stabilité en fonction de la température des agrégats obtenus avec un dépôt de 0.4 MC de Fe est examinée de 300 K à 600 K. Il est établi qu'un mûrissement de Smoluchowski a lieu à mesure que la température de recuit

Résumé

augmente et que la structure du super-réseau a entièrement disparu après un à 600 K. De plus, la désorption programmée en température de N₂ moléculairement adsorbé à 50 K sur un échantillon avec 0.4 MC de Fe déposé sur graphène/Ir(111) révèle pics de désorption à 120 K, 92 K, et 60 K. Une lente dissociation des molécules d'azote à 50 K adsorbées sur les sites d'adsorption de plus haute énergie est mise en évidence.

Mots clés : Catalyse hétérogène, nanostructures, agrégats, Fe, MgO, Ag(100), graphène, Ir(111), microscope à effet tunnel, désorption programmée en température, spectromètre de masse quadripolaire.

Contents

Abstract (English/Français)	i
1 Introduction	1
1.1 Catalysis	1
1.2 Supported metal clusters as a model catalyst	2
1.3 Ammonia synthesis	3
1.4 A motivation for bio-inspired ammonia catalysis	4
2 Experimental	7
2.1 Ultra high vacuum chamber	7
2.2 Scanning tunneling microscope	8
2.2.1 Tunneling effect	9
2.2.2 STM configuration	12
3 A highly sensitive gas detector: the sniffer	15
3.1 Thermal desorption spectroscopy	16
3.2 Quadrupole mass spectrometer	19
3.2.1 Ion source	19
3.2.2 Quadrupole mass filter	20
3.2.3 Ion detection	23
3.3 Building of the sniffer	24
3.4 Desorption of xenon from Ag(100)	27
4 Detection of Fe adatom exchange on Ag(100) by TDS investigation	31
4.1 Desorption of N ₂ from Fe/Ag(100)	32
4.2 STM topography	35
4.3 Conclusion	36
5 Fe clusters on MgO/Ag(100)	39
5.1 MgO growth on Ag(100): an STM characterization	40
5.1.1 dI/dV spectroscopy	40
5.1.2 MgO morphology	40
5.2 Thermal ripening of Fe clusters on MgO/Ag(100)	42
5.3 N ₂ on Fe clusters on MgO	46

Contents

5.4	Conclusion	47
6	Fe clusters on graphene/Ir(111)	49
6.1	Graphene on Ir(111)	49
6.2	Growth and stability investigation of Fe clusters on graphene/Ir(111) . .	51
6.3	Nitrogen desorption from Fe clusters on graphene/Ir(111)	56
6.3.1	Adsorption and slow dissociation of $^{15}\text{N}_2$ on Fe clusters	56
6.3.2	Passivation of Fe clusters by massive exposure	58
7	Conclusion	61
A	Fe flux calibration on Ir(111)	63
	Bibliography	65
	Remerciements	73
	Curriculum Vitae	75

1 Introduction

1.1 Catalysis

Catalysis refers to reaction mechanisms, induced by the presence of a material that is not consumed during the reaction, whose main characteristic is to increase the reaction rate. The presence of the catalyst has the effect of lowering the activation barrier by modifying the reaction path (figure 1.1). We distinguish two types of catalysis: homogeneous catalysis, where the catalyst and the reactants are in the same phase, and heterogeneous catalysis, where there the catalyst and the reactants are in different phases. In most cases, heterogeneous catalysts are in the solid phase and the reactants are gases.

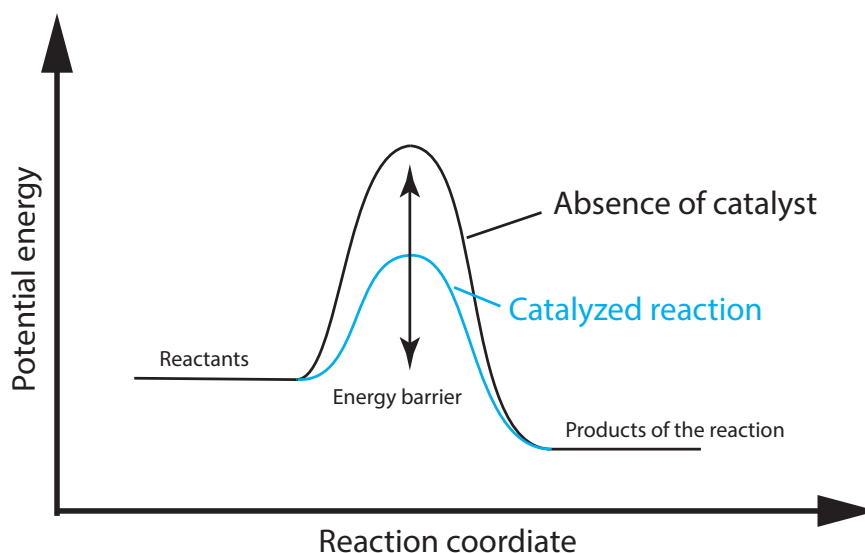


Figure 1.1 – Energy diagram of a reaction without catalyst (black path), and with a catalyst (blue path).

Catalytic performances are generally described referring to three properties. First, activity (also known as conversion rate), which describes the ability of the catalyst to increase the

reaction rate. Second, selectivity, which corresponds to the ratio of the desired products to the byproducts. These aspects have an important role in determining the reaction yield. Finally, stability, which is an essential aspect for industrial applications as it reveals the variation of activity and selectivity as a function of time. Regarding stability, catalyst deactivation is a common and complicated phenomenon which may involve for example coke formation, metal sintering, surface poisoning, catalytic structure damage.

1.2 Supported metal clusters as a model catalyst

Although heterogeneous catalysis is widely used in industry, understanding the elementary molecular processes on a working heterogeneous catalyst is challenging due to the high complexity of its structure and chemical environment. In contrast, model systems such as metallic single crystals contribute to reveal some key steps and mechanisms with well-defined atomic structures. To produce and characterize such model catalysts, surface science techniques, and especially ultra high vacuum (UHV) conditions, allow us to control the surface structure at the atomic scale, which cannot be easily achieved in ambient conditions.

Significant progress has been achieved with model systems consisting of single crystal surfaces, such as CO oxidation on Pt surfaces [1], or the Haber-Bosch process on Fe surfaces [2]. More complex model catalysts are supported metal nanoclusters. Compared to single crystal model systems, supported metal nanoclusters are closer to industrial catalysts. On the other hand, it is more challenging to reveal the structure-performance relationship since one has to take into account the metal/support interaction and other effects. A list of the effects related to the supported metal clusters has been proposed by Libuda and Freund [3]:

- **Support effects:** These consist of the different ways in which the support can influence the reaction. In some cases, the support is directly involved in the reaction. In other cases, the support is involved in the adsorbate diffusion process: the adsorbate can diffuse from the metal cluster to the support (spillover), or from the support to the cluster (reverse spillover). The support can also modify the electronic structure of the clusters and change their reactivity.
- **Electronic effects:** The limited size of the supported metal clusters makes their electronic structure significantly different than extended metal surfaces which induces different catalytic properties.
- **Geometrical effects:** These refer to the multiple facets and the increasing density of step and kink sites on the clusters which could influence the adsorption behavior of the reactants and their spatial distribution.

Additional effects can arise from the complexity of the catalyst surface morphology at the nanoscale, and the interaction between clusters:

- **Communication effects:** Adsorbates can diffuse from one region or site of the catalyst to another one. Those regions or sites can be the facets of clusters or defect sites. The spillover effect mentioned above can be considered as one of the communication effects between support and clusters.
- **Confinement phenomena:** The reaction kinetics may be affected by the limitation of the diffusion of reactants when the reactant or product is kinetically trapped in/on the catalyst, especially for porous materials such as zeolite.
- **Restructuring effects:** Adsorbate induced reconstruction or faceting are common on extended single crystal surfaces. The interaction of adsorbates with small particles may also induce changes such as modification of the clusters equilibrium shape or the bulk phase restructuring. Adsorbates can also contribute to the interaction between metal and support, which may modify structure stability and induce coarsening of the clusters.

1.3 Ammonia synthesis

The development of the industrial process for synthesizing ammonia on a large scale took place in a particular context. At the end of the 19th century, two elements urgently required this development. The first was linked to demographics. The population was rapidly increasing in Europe, and the agricultural yields saturated. This made the production of nitrogen fertilizers essential to avoid the return of famines during the 20th century, according to the demographers of the time. The second is linked to the geopolitical context that preceded the First World War. Indeed, ammonia is a precursor in the production of explosives, and the ability to synthesize it was a strategic issue.

It is in this context that F. Haber proposed a new approach with a closed-loop device and a high-pressure catalysis process. In collaboration with C. Bosch, the industrial Haber-Bosch process was developed in 1913. The search for an efficient and inexpensive catalyst was one of the priorities for the ammonia synthesis on an industrial scale. Indeed, osmium and uranium initially identified by Haber as catalysts could not be used industrially, especially because of their rarity. This task was entrusted to A. Mittasch who was the developer of the iron fused catalyst, optimized and widely used during the 20th century. The energy consumption went from 78 GJ/t for the first industrial equipment to about 27 GJ/t, with a theoretical minimum of 20.1 GJ/t. Note that most of the improvements of the catalysts used in the Haber-Bosch process have been done empirically, and many fundamentals of the mechanisms at the catalyst surface remained unknown.



Fritz Haber (1868-1934) Carl Bosch (1874-1940) Alwin Mittasch (1869-1953) Gerhard Ertl (1936-)

Figure 1.2 – Emblematic figures in the history of the development of ammonia synthesis.

The understanding of the adsorption and dissociation of nitrogen on iron, which is one of the central mechanisms of ammonia synthesis in the Haber-Bosch process, was formally described only in the 1980s by G. Ertl. His studies of chemical processes on solid surfaces were rewarded by the Nobel prize in Chemistry in 2007. The main result of Ertl *et al.* [2] is the description of the dissociative adsorption of nitrogen on Fe(111) via $N_2 \rightleftharpoons N_{2,ad} \rightarrow 2N_{ad}$. The overall sticking coefficient of the reaction is very small (about 10^{-6}).

1.4 A motivation for bio-inspired ammonia catalysis

As an integral component of all living organisms, nitrogen is an essential element in biological mechanisms. Although atmospheric nitrogen in its molecular form is an abundant source, N_2 molecules have to be dissociated and reduced to be assimilated in organisms. This process is called nitrogen fixation. The typical thermodynamic conditions in which the Haber-Bosch process takes place (500°C, 200 bar) give an idea of the difficulty to achieve nitrogen fixation under ambient conditions.

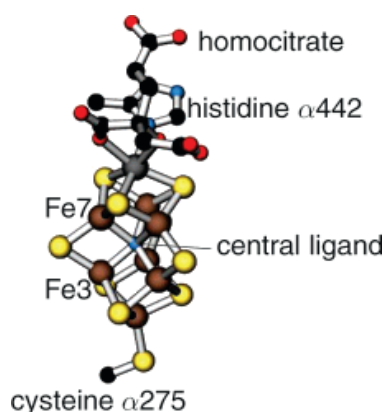


Figure 1.3 – FeMo cofactor of the nitrogenase (adapted from [4]).

1.4. A motivation for bio-inspired ammonia catalysis

The solution to this challenge found by nature is the nitrogenase enzyme present in several microorganisms called diazotrophs. This enzyme consists of two metalloproteins. The molybdenum-iron protein, where the FeMo cofactor is located, and the Fe protein, that provides electrons for the nitrogen reduction at the FeMo cofactor. The FeMo cofactor (figure 1.3) has been identified as the active site of the reaction [5,6]. Its atomic composition is one Mo atom, eight S, seven Fe, and a central ligand which can be N, O or C. Today, it is mostly admitted that this central atom is N [7].

Inspired by nitrogenase, Rod *et al.* performed density function theory (DFT) calculations for nitrogen fixation with the FeMo cofactor in the gas phase [8]. Later, Sljivancanin, Brune, and Pasquarello proposed a similar model for ammonia catalysis using an Fe₇ cluster on an oxide surface [9–11]. According to these calculations, the Fe₇ cluster has to be passivated with five N or S atoms. Then a N₂ molecule is able to chemisorb on the cluster in the molecular state and it gets decorated by H atoms until it dissociates to form a first NH₃ molecule that desorbs from the cluster. The remaining N gets subsequently decorated by an additional H atom and equally desorbs as ammonia. The capability of iron clusters to chemisorb N₂ molecules without dissociating them is surprising because on Fe surfaces the N₂ molecules dissociate and the N atoms bind so strongly that the catalyst is poisoned, unless the system is at high temperature. So the MgO(100) supported Fe₇ clusters could provide very interesting properties for ammonia synthesis at room temperature. Figure 1.4 shows the different steps during the hydrogenation of the N₂ molecule for both the nitrogenated and the sulfurized Fe₇ clusters on MgO(100).

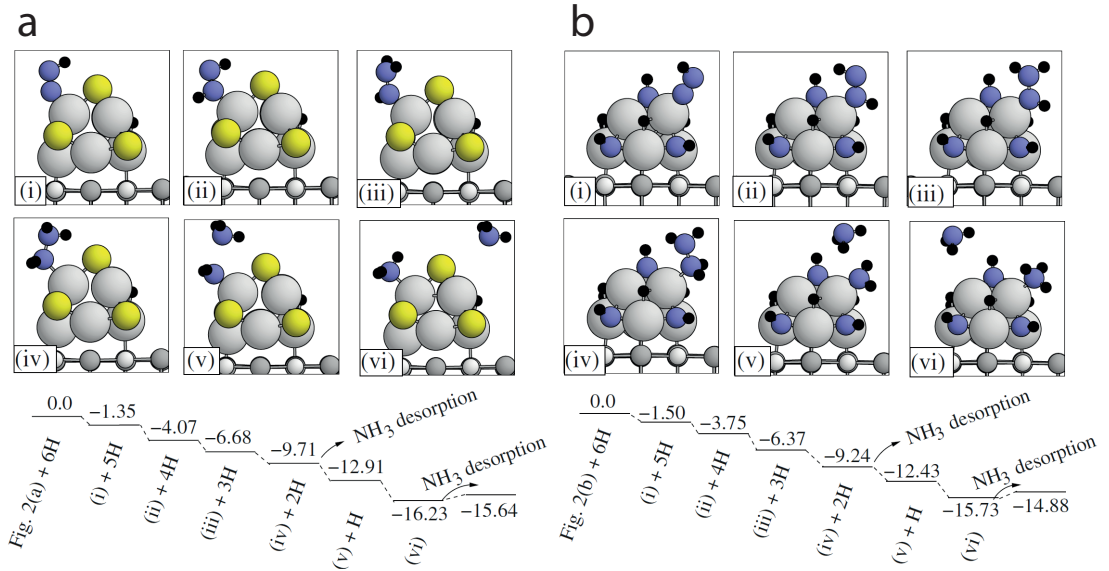


Figure 1.4 – Intermediate states during hydrogenation of the N₂ molecule for (a) the sulfurized Fe₇/MgO cluster and (b) the nitrogenated Fe₇/MgO cluster. The corresponding potential energy is displayed in both cases. The energy profile is in eV. *grey*: Fe, *blue*: N, *yellow*: S, *black*: H. (Adapted from [11])

Chapter 1. Introduction

In this thesis, we use self-assembly at surfaces [12] to grow the Fe clusters on suitable substrates. Note that an alternative method, also used in our group, consists in using a size-selected cluster source and soft-landing of these clusters onto the surface [13–15]. This strategy has the advantage of providing a mono disperse size distribution, but the location of the clusters is random. Our approach with self-assembled clusters creates a cluster size distribution with a certain width, but the advantage is that the long range order of the clusters can be controlled with a substrate that provides a template.

The general objective is to make a link between the size of the clusters and their catalytic activity. The Fe₇ clusters described above have been chosen to be investigated for that purpose as they theoretically act as a bio-inspired catalyst for one of the most essential reactions for mankind.

2 Experimental

This chapter is dedicated to the presentation of the experimental setup used in this thesis. We start with an overview of the ultra high vacuum chamber (UHV), then we give general elements about scanning tunneling microscopy (STM) and show its implementation in this system. The gas exposure and detection system (sniffer) developed during this thesis will be presented in a dedicated chapter (Chapter 3).

2.1 Ultra high vacuum chamber

The experiments performed for this project include various operations, in particular sample preparation, STM measurement, thermal desorption spectroscopy (TDS), all requiring an UHV environment ($\sim 10^{-10}$ mbar) to avoid contamination of the sample by undesirable atomic species and parasite signal during gas detection after a chemical reaction has taken place. The employed experimental setup is an already existing UHV chamber designed and built in the group [16–20]. The main feature of this chamber is its compact design: whereas lots of UHV setups are designed such that the sample preparation is performed in a dedicated chamber, our setup is composed of a unique cylindrical volume where all the operations take place. Figure 2.1a shows a schematics of the chamber with the principal instruments. The experimental setup includes an ion gun, an effusion cell, an e-beam evaporator and a heating stage for the sample preparation. The characterization instruments are the STM, the sniffer mentioned above, and an Auger spectrometer. The system is pumped by a turbomolecular pump, a Ti sublimation pump, and an ion pump. The turbomolecular pump can be isolated from the chamber and switched off during STM measurements in order to reduce vibrations. The sample sits at the center of the chamber. It is mounted on a manipulator able to rotate the sample in order to orient it in front of the installed tools that point towards the center of the chamber. The manipulator is also capable to slightly move in the x , y and z directions to adjust precisely the position of the sample. The sample holder (figure 2.1b) is thermally decoupled from Cu block by titanium screws, and is connected to the flux

cryostat with a flexible Cu braid. The sample holder attached to the Cu block can be placed on a stack of Cu plates damped against each other by viton springs. In doing so, the sample is mechanically decoupled from the environment and STM measurements can be performed. Note that the entire chamber sits on laminar flow isolators that are activated to have a second dampening stage when using the STM.

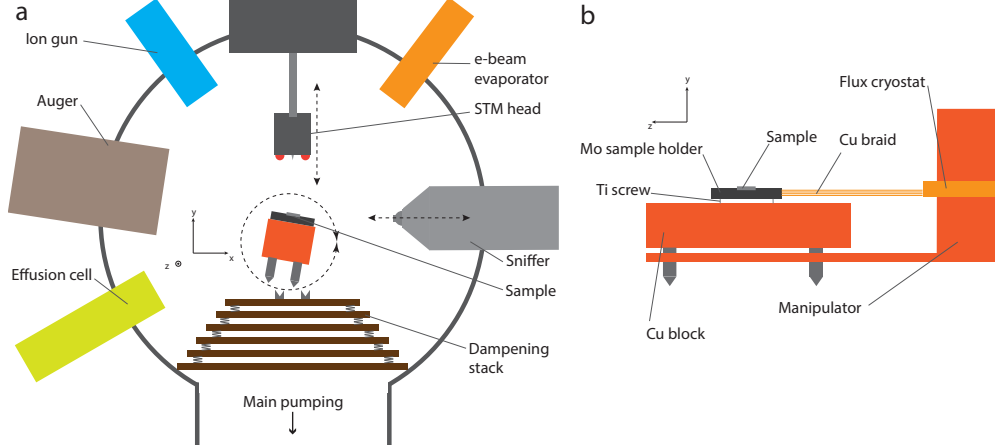


Figure 2.1 – a) Schematics of the instrumentation in the UHV chamber. b) Detail of the sample holder.

The sample temperature is measured by a Ni-Cr/Ni-Al thermocouple (Type K) that is in direct contact with it. The reference thermocouple junction is placed in a thermally regulated preamplifier. The sample can be heated by radiation and electron bombardment. Both power supplies are PID controlled and an automatic temperature control system has been implemented. The flux cryostat allows to cool the sample down to 35 K when using liquid helium.

2.2 Scanning tunneling microscope

The scanning tunneling microscope became an essential tool in surface science in the last decades. Its ability to characterize the surface morphology at the atomic level was a big step. It was invented and implemented by Binnig and Rohrer at the beginning of the 80s [22, 23]. Note that a predecessor of this instrument called topographiner was proposed 10 years earlier by Young [24]. However, it was hampered by vibrations and could not demonstrate the resolution of atomic steps. In the following decades, STM enabled many discoveries thanks to its versatility and its ability to perform spectroscopy. One recent accomplishment is the reading and writing of the magnetism of individual Ho atoms on MgO [25], making the storage of information possible in individual atoms.

The principle of operation of STM (figure 2.2a) is to approach a metallic tip, typically W, to a conductive surface at a distance of about one nanometer. By applying a small voltage between tip and sample, a current can be detected despite the absence of direct

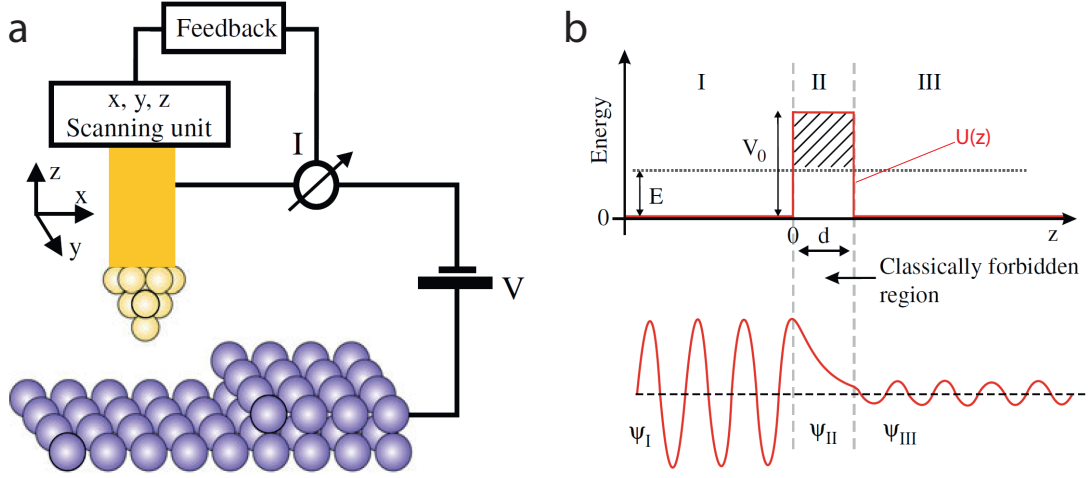


Figure 2.2 – (a) Schematic of the tip and the sample configuration in an STM. (b) Potential $U(z)$ for a metal-vacuum-metal configuration with the corresponding wave function of a particle with an energy E in the regions I, II and III: oscillating in front on the barrier, exponentially decaying inside the barrier and oscillating again with a lower amplitude past the barrier. Adapted from [21].

contact. This is the tunnel effect described in the next part. Note that to obtain a scanning probe, the tip is mounted on a scanning unit constituted of piezo elements that allow movements in the three directions. The x and y directions represent the scanning plane, and the z direction represents the height of the tip.

The most common operation mode is the constant current mode : the tip is moving in the scanning plane and the z piezo is controlled by the feedback loop in order to keep the current constant : when the tip meets an obstacle like an atomic step, a hole or an object on the surface that would change the tunneling current, the tip moves forward or backward according to the situation to correct the measured current compared to the given reference value. This mode is typically used to generate images of the surface topography of a sample. In our catalysis project we operate the STM mostly in the constant current mode for surface characterization.

2.2.1 Tunneling effect

In this part, we give a basic derivation of the expression for the tunneling current. A more complete description of the STM technique including theoretical and operational aspects can be found in the book of C. Julian Chen [26] and in the book of Bert Voigtländer [21].

The tunneling effect is a quantum mechanical concept that can be described in a one-dimensional model. We consider an electron with an energy E moving in a potential $U(z)$.

Chapter 2. Experimental

The electron is described by a wave function $\psi(z)$ satisfying the Schrödinger equation :

$$-\frac{\hbar^2}{2m} \frac{d^2}{dz^2} \psi(z) + U(z)\psi(z) = E\psi(z) \quad (2.1)$$

The case of an STM tip in tunneling contact with the sample can be represented by a metal-vacuum-metal junction forming an energy barrier V_0 whose height corresponds to the vacuum level as shown in figure 2.2b. The solution of equation 2.1 in the crystal (regions I and III where $E > U(z)$) is given by:

$$\psi(z) = \psi(0)e^{\pm ikz} \quad \text{with } k = \frac{\sqrt{2m(E - U(z))}}{\hbar} \quad (2.2)$$

corresponding to an oscillating wave function.

An electron from the surface at the Fermi level, *i.e.*, the occupied state with the highest energy E_F , has an energy lower than the vacuum level: $E_F < V_0$. In classical mechanics it means that the electron is trapped in the metal and cannot pass through the energetic barrier and be located in the vacuum. The work function ϕ of a metal surface is defined as the minimal energy required to remove an electron from the bulk to the vacuum level. Then, we obtain the relation $\phi = V_0 - E_F$. For materials commonly used in STM, the work function is typically 4-5 eV. In a general STM configuration tip-vacuum-sample with different work functions ϕ_{tip} and ϕ_{sample} for the tip and the sample, respectively, we approximate the height of a trapezoidal barrier by a rectangular barrier with the average height of the trapezoidal barrier (figure 2.3a): $\bar{\phi} = (\phi_{\text{tip}} + \phi_{\text{sample}})/2$. The solution of the Schrödinger equation in the vacuum region is:

$$\psi(z) = \psi(0)e^{-\kappa z} \quad \text{with } \kappa = \frac{\sqrt{2m\bar{\phi}}}{\hbar} \quad (2.3)$$

This expression describes the decay of the wave function into vacuum. From the solution 2.3 we can obtain the probability density w for an electron at the Fermi level, to be located at a position z in vacuum:

$$w \propto |\psi(z)|^2 = |\psi(0)|^2 e^{-2\kappa z} \quad (2.4)$$

In other words, the probability to find the electron in vacuum decreases exponentially with the distance. Consider now the tip at a distance d from the sample. According to equation 2.4, there is non-zero probability of finding the electron at the position of the

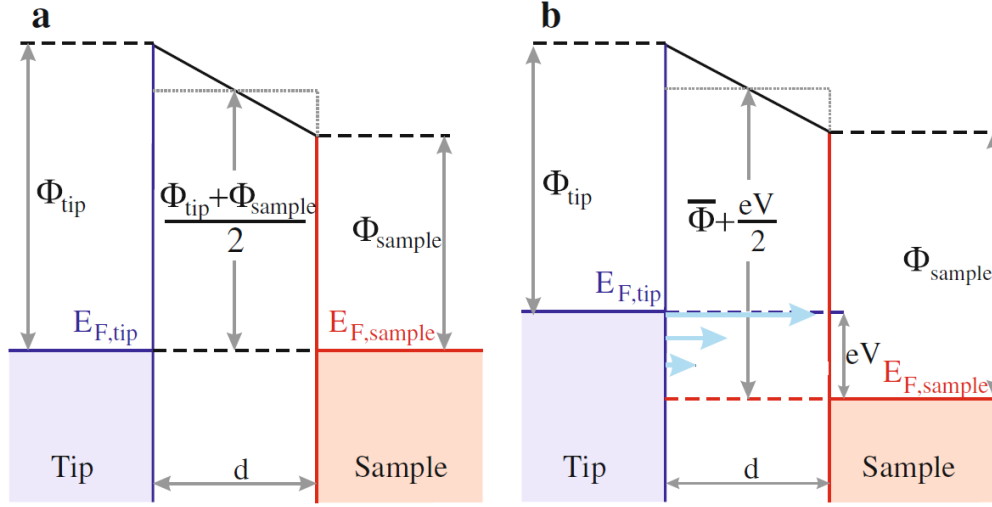


Figure 2.3 – a) Energy diagram with no bias applied. The Fermi levels of tip and sample are aligned. b) Energy diagram with a positive bias applied to the sample. Adapted from [21].

tip, meaning that an electron transfer between the two metallic regions is possible. In the absence of a bias, the transmission is symmetrical in both directions, leading to a zero net flow (figure 2.3a). In the presence of a bias V , a net tunneling current appears. The effect of the bias is to shift upward or downward the states according to the sign of the voltage (figure 2.3b). Then, all the occupied states ψ_n of energy E_n included in the interval $[E_F - eV, E_F]$ in one electrode, and all the unoccupied states of the other electrode with $[E_F, E_F + eV]$, contribute to the net flow. Note that the bias also changes the height of the effective barrier, which becomes:

$$\phi_{\text{eff}} = \frac{\phi_{\text{tip}} + \phi_{\text{sample}}}{2} + \frac{eV}{2} \quad (2.5)$$

and we define:

$$\kappa_{\text{eff}} = \frac{\sqrt{2m\phi_{\text{eff}}}}{\hbar} \quad (2.6)$$

By replacing κ with κ_{eff} in equation 2.4, we can express the tunneling current as:

$$I \propto \sum_{E_n=E_F-eV}^{E_F} |\psi_n(0)|^2 e^{-2\kappa_{\text{eff}}d} \quad (2.7)$$

The exponential relation of the tunneling current with the distance d between the tip

Chapter 2. Experimental

and the sample gives the STM a very high resolution in the z direction.

For a small enough bias, the density of electronic states does not vary significantly in the expression 2.7. Then it is more convenient to write the sum in terms of local density of states (LDOS) at the Fermi level. The LDOS $\rho(z, E)$ is defined at a position z and at an energy E as:

$$\rho(z, E) \equiv \frac{1}{\epsilon} \sum_{E_n=E-\epsilon}^E |\psi_n(z)|^2 \quad (2.8)$$

with ϵ small enough. According to this definition, the sum in equation 2.7 can be written in terms of sample LDOS ρ_S at E_F at the tip position $z = d$:

$$\sum_{E_n=E_F-eV}^{E_F} |\psi_n(0)|^2 e^{-2\kappa_{\text{eff}}d} = \rho_S(d, E_F)eV \quad (2.9)$$

Finally, the current can be conveniently expressed in term of the LDOS :

$$I \propto \rho_S(d, E_F)V \quad (2.10)$$

According to equation 2.10, an STM image generated in constant current mode is a contour of constant LDOS at E_F of the sample surface. The apparent height of objects and regions on an STM image are not only given by the morphology, but also by their electronic properties.

2.2.2 STM configuration

In this work, we use a variable temperature STM that has been specifically designed for this UHV chamber. Details can be found in Weiss's thesis [27]. The compact STM head includes all the piezo elements for scanning. It is mounted on a manipulator that can move up and down. For the STM measurements, the sample holder is placed on the dampening stack (figure 2.4a) and the STM head is placed on the helical ramps that surround the sample (figure 2.4b). For approaching the tip, the shear-piezoes attached to the feet of the STM head are activated by means of a sawtooth voltage that makes the head rotate on the ramps downwards until the tunneling junction between the tip and the sample is established.

The STM allows the sample to be measured in a large temperature range. In this work we use it typically from room temperature down to 50 K. The thermal stability of the

2.2. Scanning tunneling microscope

sample is essential when imaging to avoid thermal drift that disturbs the measurement. The PID temperature controller allows to keep the sample at a fixed temperature with very low fluctuations, about 0.05 K. When operating at low temperature, about two hours are required to thermalize the STM head via the feet that are in contact with the cold ramps. Even, after this delay, the thermal drift is still significant and must be taken into account when analysing the STM images.

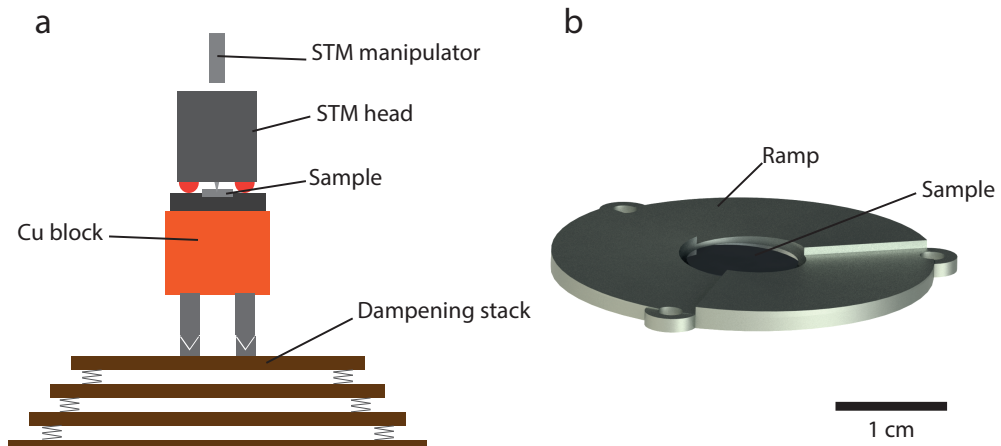


Figure 2.4 – a) Schematic of the STM in scanning position with the sample positioned on the dampening stack. b) Detail of the ramps used for coarse approach of the tip to the sample.

3 A highly sensitive gas detector: the sniffer

The study of the catalytic properties of nanoparticles such as Fe clusters requires a measuring device capable of detecting reaction products while dosing the gases. Since the surface of the nanoparticles is orders of magnitude smaller than the chamber walls, or other components of the UHV system, this detection and dosage have to be performed in a highly selective way exposing the particles only. We have built a highly sensitive gas detector that satisfies these requirements. It is based on a design developed in our group [13–15]. The new version includes several modifications made to adapt it to the UHV setup presented in the previous chapter. The main idea behind the sniffer is to obtain a volume, almost isolated from the main chamber, in which the surface where the reaction takes place is located. The goal is to screen the surface of interest from any other reactive surface. Concomitantly, the gas in this volume is analyzed by a mass spectrometer. The reaction takes place at the surface, the goal is to screen the surface from any other reactive surface which we also expose to the reactants, therefore the surface seen by the reactants have to be i) our surface of interest ii) other surfaces that are non-reactive. We achieve this by sealing the exposure and detection volume with respect to the chamber and by having in this volume only materials that are inert, apart from the surface of interest.

The construction of this instrument is motivated by the specificities of the catalysis project. According to the initial proposal, which consists in testing the catalytic activity of Fe₇ clusters on an MgO surface, the detector must be able to perform thermal desorption measurements of molecules adsorbed on these clusters. The typical cluster density is of the order of 1% of the atomic density of the substrate. Assuming for example that one molecule is attached to each cluster, the detector should be able to detect the desorption of a coverage of the order of 0.01 ML of gas during the desorption experiment (1 ML being defined generally as one adsorbed molecule per substrate unit cell). The detection threshold depends on several factors: the signal-to-noise ratio of the gas analyzer, the background level for the mass being analyzed, the geometry of the system being defined by the volume in which the gas desorbs, and the pumping speed of this volume. Concerning

the last point, the sniffer is based on the concept developed by Feulner and Menzel [28], *i.e.*, a reduced volume with dedicated pumping. The partial pressure p of a gas in the sniffer can be expressed by the following equation according to Redhead [29]:

$$\frac{dp}{dt} + \frac{p}{\tau} = aN(t) \quad (3.1)$$

where :

- $N(t)$ is the desorption rate in molecules/cm² s.
- $\tau = V/S$ is the characteristic pumping time with V the volume of desorption, and S the pumping speed in l/s.
- $a = A/KV$, with A the sample area in cm² and $K = 3.27 \cdot 10^{19}$ molecules/l torr at 295 K.

The aim is to have τ small enough such that p/τ is the dominant term in equation 3.1. In this way, the measured pressure is proportional to the desorption rate $N(t)$. To achieve this condition, for a given desorption volume V , a compromise for the pumping speed S must be found between the sniffer sensitivity and the characteristic time.

In this chapter, we first describe the theory of thermal desorption spectroscopy. Next, we describe the general principles of a quadrupole mass spectrometer (QMS). Then we detail the construction of the sniffer. Finally, we present test measurements performed to verify the operation of the device.

3.1 Thermal desorption spectroscopy

Thermal desorption spectroscopy (TDS) or temperature programmed desorption (TPD) is an experimental method to observe the desorption of molecules from a surface when its temperature increases. In the following, we consider a linear temperature ramp $T = T_0 + \beta t$. The desorption rate $N(t)$ is expressed by a rate law of n^{th} order :

$$N(t) = -\frac{d\sigma}{dt} = k_n \cdot \sigma^n \quad (3.2)$$

where σ is the coverage in molecules/cm² and k_n the rate constant described by an Arrhenius equation:

$$k_n = \nu_n \cdot \exp\left(-\frac{E_d}{RT}\right) \quad (3.3)$$

where E_d is the activation energy for desorption and ν_n the prefactor. By replacing 3.3 in 3.2, we get the so-called Polanyi-Wigner equation:

$$N(T) = -\frac{d\sigma}{dt} = \nu_n \sigma^n \cdot \exp\left(-\frac{E_d}{RT}\right) \quad (3.4)$$

In equation 3.4, the activation parameters E_d and ν_n are supposed to be independent of coverage. The order of desorption n is determined by the mechanisms occurring at the surface and involved in the desorption. Figure 3.1 shows the typical peak shape obtained for $n = 0, 1, 2$. In zero-order kinetics, the desorption rate is independent of coverage and increases as a function of temperature until there are no absorbed molecules anymore. The desorption of molecules from a 2D gas phase at the surface in equilibrium with a condensates 2D phase exhibits zero-order kinetics: the gas phase is supplied by the molecules from 2D phase and the equilibrium is sustained as long as there are condensate islands at the surface. Increasing the initial coverage pushes the temperature of the maximum desorption rate to the right (figure 3.1a). In first-order kinetics, the molecules possibly diffuse, and desorb without interaction with others. Then, the desorption rate is proportional to the coverage σ and increasing the initial coverage does not change the temperature of the maximum desorption rate (figure 3.1b). The second-order kinetics requires the recombination of two species so at least one must diffuse before the product of the reaction desorbs. In this case, increasing the initial coverage increases the probability of recombination and the temperature of the maximum desorption rate is shifted the left (figure 3.1c).

In the following, we present the usual analysis methods for zero-order and first-order peaks.

For zero-order desorption ($n = 0$), taking the logarithm of equation 3.4 gives:

$$\ln(N(T)) = \ln(\nu_0) - \frac{E_d}{R} \cdot \frac{1}{T} \quad (3.5)$$

The desorption energy E_d and the prefactor can be directly extracted by plotting the desorption spectra in an Arrhenius plot ($\ln(N(T))$ vs $1/T$).

For first-order desorption kinetics ($n = 1$), equation 3.4 provides an expression linking the desorption energy E_d , the prefactor ν_1 , and the temperature T_p at which the desorption rate is maximum. We first substitute the time t in the Polanyi-Wigner equation by $dt = (1/\beta) \cdot dT$. Furthermore the condition $dN(T_p)/dT = 0$ must be fulfilled at the

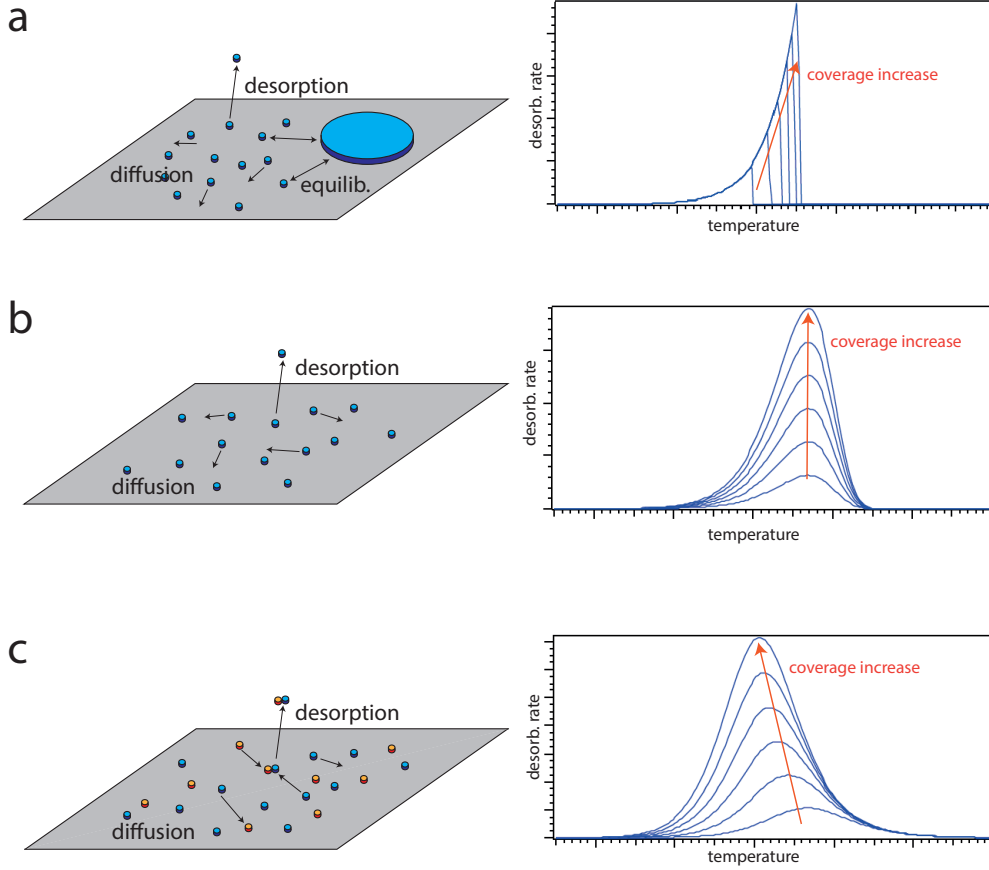


Figure 3.1 – a) Typical surface mechanisms and corresponding desorption peak shape with various coverages for a) Zero-order desorption. b) First-order desorption. c) Second-order desorption.

maximum desorption rate. The expression obtained is:

$$\frac{E_d}{RT_p^2} = \frac{\nu_1}{\beta} \exp\left(-\frac{E_d}{RT_p}\right) \quad (3.6)$$

From equation 3.6, Redhead [29] proposed a relation to estimate E_d from T_p , assuming a value for ν_1 , typically $\nu_1 = 10^{13} \text{ s}^{-1}$:

$$E_d = RT_p \left[\ln \frac{\nu_1 \cdot T_p}{\beta} - \ln \frac{E_d}{RT_p} \right] \quad (3.7)$$

The second term in brackets is small relative to the first and its estimation gives 3.64.

The equation 3.7 becomes:

$$E_d = RT_p \left[\ln \frac{\nu_1 \cdot T_p}{\beta} - 3.64 \right] \quad (3.8)$$

This approximation introduces an estimated error of less than 1.5% for $10^{13} > \nu_1/\beta > 10^8 \text{ K}^{-1}$.

In order to determine E_d without assuming a value for ν_1 , it is possible to use the heating rate variation method. A series of desorption spectra with different heating rates β is measured. From each spectrum, the temperature of the maximum desorption rate T_p is determined. From 3.6, taking the logarithm, some rearrangement yields:

$$\ln \frac{T_p^2}{\beta} = \frac{E_d}{RT_p} + \ln \frac{E_d}{\nu_1 R} \quad (3.9)$$

From 3.9, the desorption parameters can be determined by plotting $\ln(T_p^2/\beta)$ vs $1/T_p$ for the different β values. E_d is deduced from the slope, and the prefactor ν_1 from the intercept with the ordinate.

3.2 Quadrupole mass spectrometer

3.2.1 Ion source

A quadrupole mass filter requires the molecules to be ionized before they enter it. This is done by electron bombardment in a part referred as ion source. The ion source used here is shown in figure 3.2a. The electrons are produced by an yttriated iridium hot cathode (filament). They are accelerated from the cathode to the grid that acts as anode at an energy between typically 100 eV and 150 eV, which corresponds to the maximum of the ionization cross section for most of the molecules considered in this work (figure 3.2b). The electrons pass through the grid and reach the ionization volume.

At low pressure, the electron mean free path is large enough compared to the size of the ionizer and the ion current I_{K+} of a gas component K can be expressed as:

$$I_{K+} \propto i_{e-} \cdot \sigma_{K+} \cdot p_K \quad (3.10)$$

where i_{e-} is the electron current, σ_{K+} is the ionization cross section (single ionization) of the component K , and p_K is the partial pressure of the gas component K .

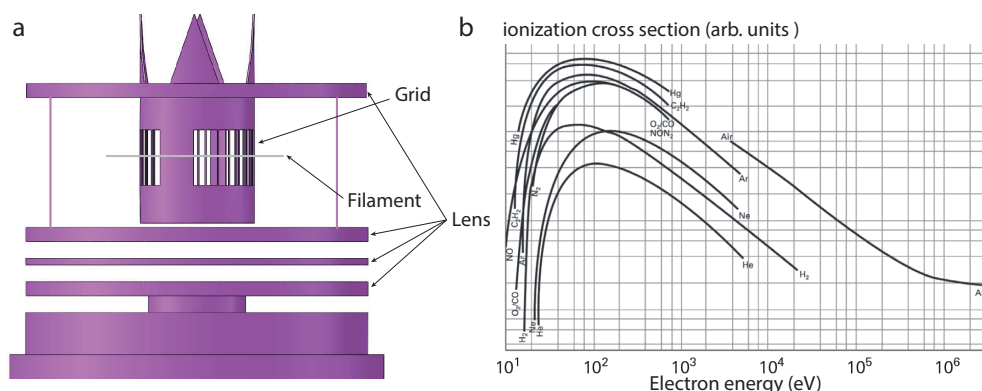


Figure 3.2 – a) Sketch of the open ion source used here. b) Ionization cross section for various common gases (adapted from Pfeiffer database).

In quadrupole mass spectroscopy, a molecule K is not only detected with its single ionization. Multiple charged ions K^{n+} occur by the same mechanism than single ionization but with a different and generally much smaller cross section. Furthermore, molecules can be fragmented down from parent molecules. Thus, the ionization of a single gas component produces a variety of ions with different respective proportions. The resulting mass spectrum is its signature. To obtain this mass spectrum, the ions have to be filtered as function of their mass to charge ratio m/e . The ions reach the mass filter after passing through a set of focalization lenses.

3.2.2 Quadrupole mass filter

The following section describes the mass selection in a quadrupole mass filter (QMF). More details about quadrupoles can be found in Campana’s paper [30] and in the Gerlich’s book [31].

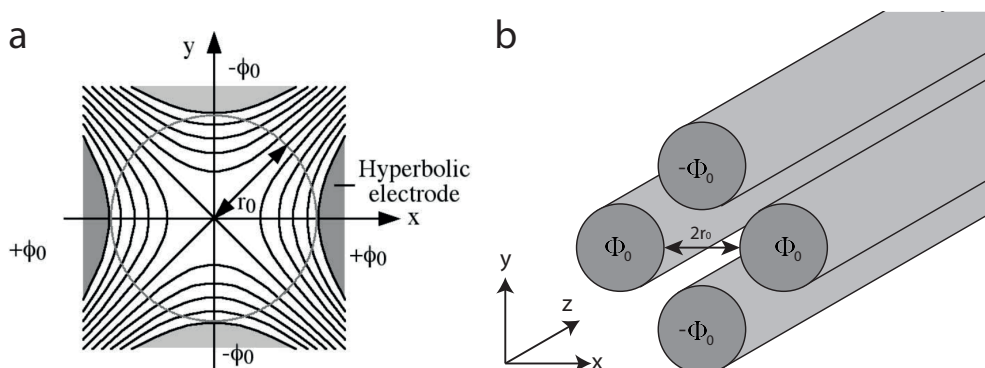


Figure 3.3 – a) Hyperbolic electric potential ϕ generated by an ideal quadrupole (adapted from [32]). b) Section of a quadrupole mass filter.

3.2. Quadrupole mass spectrometer

To understand the mass filtration mechanism, one starts from the hyperbolic electric potential generated by an ideal quadrupole. This potential is expressed in the (x,y) plane perpendicular to the quadrupole electrodes as :

$$\phi(x, y) = \phi_0 \frac{(x^2 - y^2)}{r_0^2} \quad (3.11)$$

where ϕ_0 is the potential applied to the hyperbolic shaped electrodes, and r_0 is the radius of the inscribed circle between the four electrodes. Note that in commercial QMFs, the hyperbolic electrodes are generally replaced by cylindrical rods (figure 3.3b) yielding fields similar to the ideal quadrupole field.

In a quadrupole mass spectrometer, the potential applied to the electrodes is the sum of a DC voltage U and a RF voltage $V \cos(\omega t)$

$$\phi_0 = U + V \cos(\omega t) \quad (3.12)$$

where V is the amplitude of the oscillation and ω is the angular frequency. The potential equation becomes:

$$\phi(x, y) = (U + V \cos(\omega t)) \frac{(x^2 - y^2)}{r_0^2} \quad (3.13)$$

The resulting electric field is:

$$\begin{cases} E_x = -\frac{\partial \phi(x,y)}{\partial x} = -\frac{2}{r_0^2} (U + V \cos \omega t) x \\ E_y = -\frac{\partial \phi(x,y)}{\partial y} = +\frac{2}{r_0^2} (U + V \cos \omega t) y \end{cases} \quad (3.14)$$

The equations of motion of an ion with mass m and charge e are:

$$\begin{cases} \frac{d^2 x}{dt^2} + \frac{2e}{mr_0^2} (U + V \cos \omega t) x = 0 \\ \frac{d^2 y}{dt^2} - \frac{2e}{mr_0^2} (U + V \cos \omega t) y = 0 \end{cases} \quad (3.15)$$

We introduce the following dimensionless substitutions, where μ represents either x or y :

$$\xi = \frac{\omega t}{2} \quad (3.16)$$

$$a = a_x = -a_y = \frac{8eU}{mr_0^2\omega^2} \quad (3.17)$$

$$q = q_x = -q_y = \frac{4eV}{mr_0^2\omega^2} \quad (3.18)$$

The equations of motion become:

$$\frac{d^2\mu}{d\xi^2} + (a_\mu + 2q_\mu \cos 2\xi) \mu = 0 \quad (3.19)$$

Equation 3.19 is a well known differential equation called Mathieu equation. Its solutions are:

$$\mu(\xi) = A \cdot \sum_{n=-\infty}^{\infty} C_{2n} \cos(2n + \beta) + B \cdot \sum_{n=-\infty}^{\infty} C_{2n} \sin(2n + \beta) \quad (3.20)$$

A and B are determined from boundary conditions μ , $d\mu/d\xi$, and ω . C_{2n} and β are functions of a and q . Stable solutions 3.20 of the Mathieu equation describing a QMF give the stable trajectories of an ion through the length of the quadrupole field. For an ion with a fixed mass-to-charge ratio m/e , they can be represented in the (a, q) space by a stability region diagram (figure 3.4).

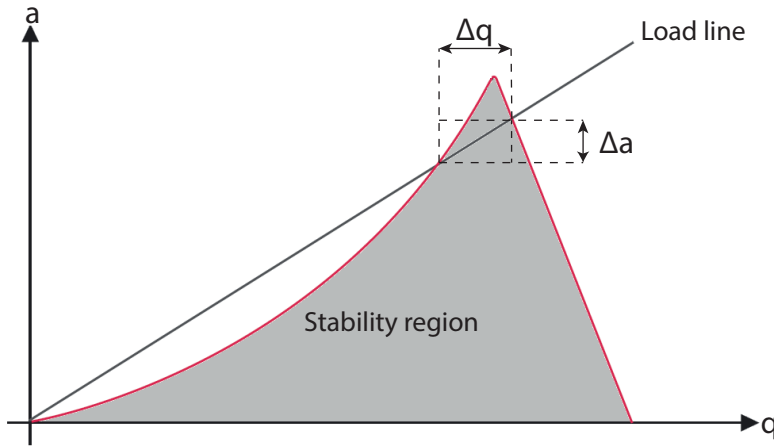


Figure 3.4 – Stability region diagram of a QMF.

During a mass scan, U and V are changed in order to vary the parameters a and q along the so-called load line. To obtain a mass spectrum, the load line has to be tuned in

such a way that it passes through the different stability regions corresponding to the respective m/e ratios. In doing so, the area delimited by the load line at the apex of the stability region corresponds to the ions transmitted through the QMF. Note that in a mass spectrum, the peaks are designated by the atomic mass number corresponding to a single-ionized ion.

The mass resolution is defined as $R = m/\Delta m$. The following relation between U , V and R can be derived:

$$s = \frac{a}{q} = \frac{2U}{V} = \frac{\Delta a}{\Delta q} = \frac{a}{\Delta q R} \quad (3.21)$$

where s is the slope of the load line, and Δa and Δq represent the distance of the points of intersection of the load line and the stability region boundaries. In constant resolution mode, R determines the ratio U/V , and thus, the slope of the load line.

Note that in the Pfeiffer quadrupole used in the gas detector, the ratio U/V is varied as a function of the mass number such that the resolution $m/\Delta m$ does not remain constant, but instead the line width Δm remains constant. In other words, the actual mass resolution increases proportionally to the mass number.

3.2.3 Ion detection

At the exit of the mass filter, the selected ions are captured by the ion current measuring device. Two different detectors are installed on the Pfeiffer mass spectrometer and can be used depending on the situation. The first and simplest is a Faraday cup. This is a simple collector onto which the ions transfer their electrical charges. The current thus created is converted into voltage by a current to voltage converter. This device has the advantage of being robust and stable over the long term. However, it does not allow the detection of very low partial pressures. The theoretical detection limit is of the order of 10^{-10} mbar. In practice, below 10^{-8} mbar, we use a second detector allowing to drastically increase the sensitivity.

This detector (figure 3.5) is a continuous secondary electron multiplier (C-SEM) also called channeltron. It consists of a glass tube coated with a high-resistance conductive layer with a low work function. A high negative voltage is applied at the inlet so that a uniform voltage gradient is established along the tube. Ions from the mass filter are routed to a conversion dynode to generate secondary electrons. Those electrons enter into the glass tube and start an electron avalanche. The e^- current at the end of the tube is measured by a conventional electrometer amplifier.

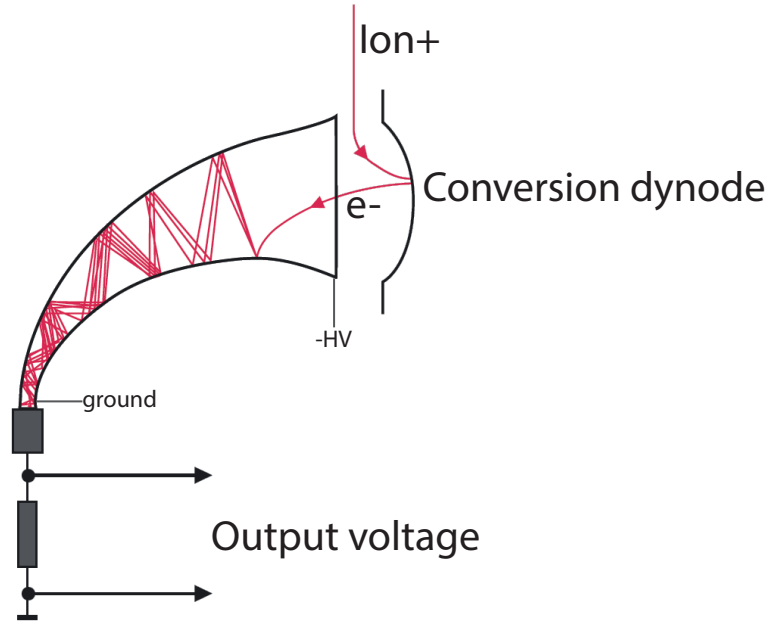


Figure 3.5 – Operating principle of continuous secondary electron multiplier.

3.3 Building of the sniffer

In the following we describe the new version of the sniffer, compatible with the experimental setup outlined in chapter 2. The technical drawing in figure 3.6 shows the sniffer with all its components.

We start from a commercial QMS (Model QMA 200 from Pfeiffer Vacuum). In order to create a reduced and almost closed desorption volume, the original ion source (figure 3.2a) is modified by adding a tube with only a small opening for electron injection. The desorption volume consists essentially of a quartz tube with an orientable nose at one end against which the sample is placed, and the QMS at the other end. The nose adjusts itself to the orientation of the sample, a procedure which allows to close and isolate the desorption volume from the main chamber. The volume indicated in dotted lines in figure 3.6, including the quartz tube and the ionizer, is the desorption volume. This volume V is about 6200 mm^3 . Pumping is performed through the slit of the ionizer (1.6 mm^2) and the hole of the quadrupole (3 mm^2). The corresponding characteristic time τ can be calculated with:

$$\tau = \frac{V}{S} \quad (3.22)$$

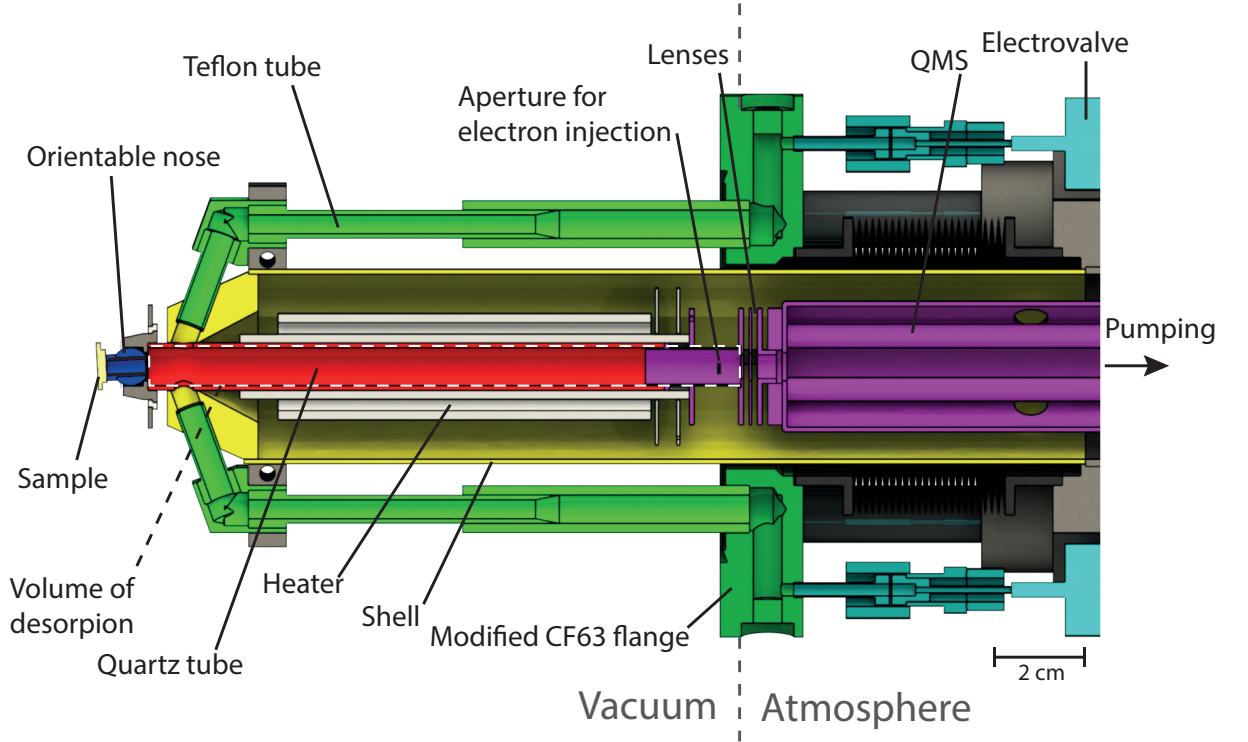


Figure 3.6 – Longitudinal cut of the sniffer.

where S is the pumping speed in mm^3/s . This pumping speed is:

$$S = A \sqrt{\frac{k_B T}{2\pi m}} \quad (3.23)$$

where A is the total pumping surface, m is the mass of the molecule, k_B is the Boltzmann constant, and T the temperature. For a gas of atomic mass $m = 28$ amu at a temperature of 300 K, the characteristic time is time $\tau = 11$ ms.

One of the conditions to obtain high sensitivity is to maintain the lowest possible background pressure in the sniffer, *i.e.*, to have a clean and degassed system. To achieve this, the quartz tube is surrounded by a ceramic heater which allows the surrounding surfaces to be degassed beforehand. The use of quartz for the collector tube also contributes to this goal, since it is a very pure and clean material that does not release unwanted gases. Another point that must be taken into account for a catalysis experiment is that one wants to avoid having parasitic reactions, and quartz also has an advantage for this because it is chemically inert. This is also the reason why the filament is placed outside the desorption volume. In this way the gases present in the desorption volume are not in direct contact with the filament, which could also generate parasitic reactions. Note that heating the volume of desorption is also useful when using sticky gases like

Chapter 3. A highly sensitive gas detector: the sniffer

CO or O₂, since the residence time τ_r of molecules on the wall of the tube increases significantly the characteristic time τ . Heating them reduces the adsorption.

All these elements are located in a closed shell with a dedicated pumping stage (345 l/s for N₂) in order to make the desorption volume and the reactions that take place there as independent as possible from the main chamber.

Another feature of the sniffer is the possibility to expose the sample to a controlled amount of gas. Two independent electromagnetic pulsed valves (Parker, model 099-0340-900) are connected to the collector volume in which the sample is located. In this new version of the sniffer we use Teflon tubes with a sliding design positioned outside the shell. The use of Teflon is motivated by two arguments. First, Teflon is chemically inert and therefore expected to minimize the residence time of molecules on its surface which is particularly important for gases that have a high surface adsorption energy (O₂, CO). Second, its self-lubricant property allows to use the sliding design required for the integration of the sniffer in the UHV chamber.

The gas pulses are controlled by a rectangular voltage pulse of typically 1 - 4 μ s duration and 20 - 30 V amplitude, corresponding to a partial opening of the electrovalve. We fill the gasline connected to the electrovalve with the specific gas used in the experiment at a typical pressure of 10 mbar. The gasline serves as a reservoir to supply the electrovalve. A lower pressure in the gasline means that a larger opening of the electrovalve is necessary to obtain the desired peaks, which allows a greater regularity of the pulses. However, this also increases the relative contamination of the gas. The gaslines are initially pumped at a pressure below the limit value of the gauge ($5 \cdot 10^{-4}$ mbar). After closing the pumping, the pressure increases to the low 10^{-3} mbar within a few hours. Therefore, the relative contamination of the gas should not exceed 10^{-4} in the time of the experiment. The pressure in the gasline is measured by a Pirani gauge (Pfeiffer TPR 280). Depending on the gas, the reading has to be corrected according to the tables provided by the manufacturer.

An inspection of the internal geometry of the electrovalves revealed the existence of a large dead volume (figure 3.7a). We decided to reverse the mounting by swapping the input and the output ports with respect to the instruction of the supplier (figure 3.7b). This does not compromise the sealing of the valves because the typical used pressure creates a negligible force. This small modification has a huge impact on the time resolution of the sniffer given by the exponential temporal decay of the pressure after the peak: xenon pulses obtained with the valve mounted in the original position and in reversed position give the respective time constant of 920 ms and 210 ms (figure 3.7c). Better time resolution should not affect thermal desorption experiments but it increases the performance for experiments addressing kinetics [13, 33–35].

3.4. Desorption of xenon from Ag(100)

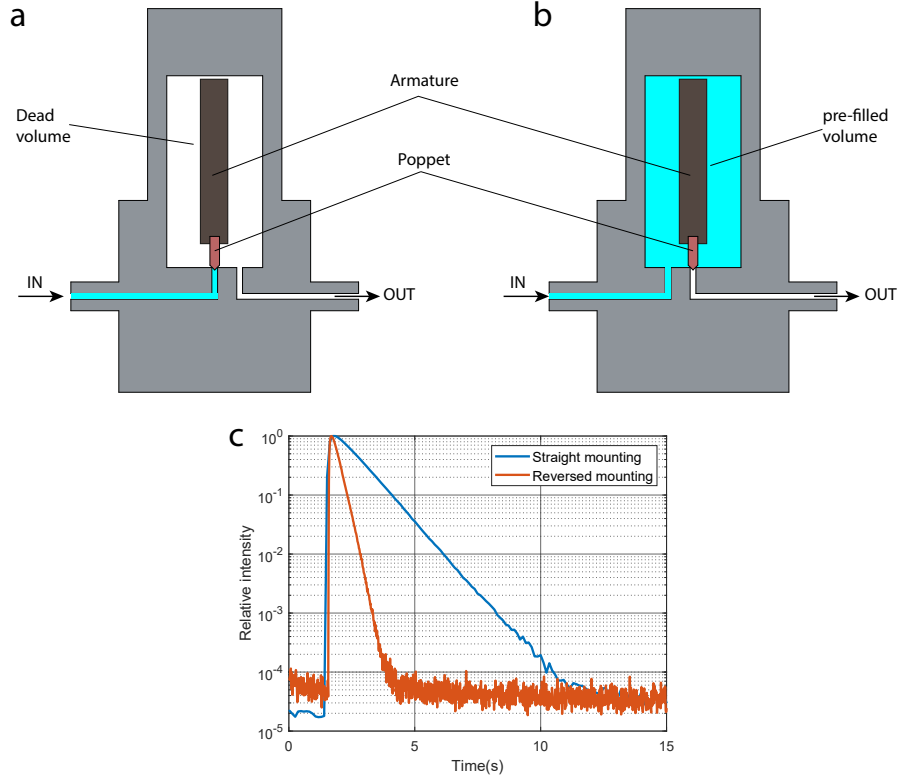


Figure 3.7 – Sketch of the electrovalves in a) the mounting recommended by the manufacturer and in b) the reversed mounting. The parts that allow the poppet to move (frame, spring) are not shown here. c) Comparison between the xenon pulse decay obtained with the electrovalve in the original position and in the reversed one. The integration time between measurement points, respectively 100 ms and 10 ms, explains the higher noise in the background signal in the second case.

3.4 Desorption of xenon from Ag(100)

We tested the dynamical range of the sniffer with TDS of xenon adsorbed on a clean Ag(100) surface. The crystal was prepared with repeated cycles of Ar^+ sputtering (1200 eV, $2.6 \mu\text{A}/\text{cm}^2$, 300 K) and annealing at 850 K for 15 min followed by a controlled cooling with a rate of 1 K/s to 500 K that yields several hundred nanometers wide clean terraces as verified by means of STM. The surface is exposed to xenon at 36 K. Since the controller of the mass spectrometer does not allow to select masses higher than 100 amu, we record mass 66 that corresponds to the double ionization of the main xenon isotope. According to tabulated data, the resulting signal is about one order of magnitude smaller than the one expected for the first ionization but still large enough to provide the large dynamic range shown below.

Figure 3.8 shows the TDS obtained for various Xe coverages, in linear and in logarithmic scale. The heating rate was 0.5 K/s. The Xe exposure ranged from 0.0023 to 24 L (1

Langmuir (L) corresponds to an exposure of $1 \cdot 10^{-6}$ Torr during 1 s). At the maximum exposure, three peaks are visible in the spectrum, and correspond to the desorption of atoms belonging to three different Xe layers. The peak appearing between 80 and 90 K originates from desorption of Xe atoms in the first layer (directly in contact with the Ag substrate), the one between 60 and 70 K from desorption of atoms in the second layer, when present. Note that the first layer is by far not saturated when the second layer starts to form. For the highest exposure, a third peak at slightly lower temperature develops, corresponding to desorption of Xe atoms of the third layer. The indicated coverages are calculated from the integral of the desorption spectra. In particular, one ML is defined as the area of the first monolayer peak in the spectrum obtained with the largest exposure, since this corresponds to the signal of the desorption of a saturated Xe monolayer. The leading edge of those peaks are straight lines in the Arrhenius plot. The signal decreases suddenly after the maximum. This peak shape suggests zero-order desorption (rate $\sim \nu_0 e^{-E_d/kT}$). It is indicative of a 2D gas-condensate coexistence: the molecules desorb from the 2D gas phase which is supplied by the continuous attachment-detachment process of the atoms at the edges of Xe islands. This behavior has already been reported for rare gases physisorbed on clean metal surfaces [36–39].

The quantitative analysis of the first layer peak in the Arrhenius plot (figure 3.8c) for coverages from 0.27 ML to 2 ML gives a desorption energy E_d in the range 0.22 – 0.23 eV and a prefactor ν_0 between $4 \times 10^{12} \text{ s}^{-1}$ and $1 \times 10^{13} \text{ s}^{-1}$. For comparison, Behm *et al.* obtained a desorption energy $E_d = 0.225 \text{ eV}$ and a prefactor $\nu_0 = 3 \times 10^{15} \text{ s}^{-1}$ for Xe/Ag(111) [36]. Therefore our results are in very good agreement with the value of activation energy reported in the literature for a closely-related system. The signal of the desorption peak corresponding to the first saturated layer covers six orders of magnitude, showing the very large dynamical range of our setup. Similar performances were obtained by Widdra *et al.* with the Feulner cap design [38]. At the lowest coverage used in our experiment, the desorption peak still spans more than one order of magnitude.

At very low coverage ($\theta < 0.01 \text{ ML}$) the desorption does not follow the same zero-order mechanism described above: the peak starts at 70 K with the lowest exposure. With increasing coverage, the peak tends to the zero-order regime described above. One qualitative explanation could be the adsorption of Xe atoms on sites corresponding to point defects or structural defects such as steps at the surface. Those sites correspond generally to higher adsorption energies. Thus, the atoms at the surface attach first to those sites until they are saturated [38]. Consequently, at low coverage, atom desorption from defects and steps dominates.

In conclusion, this chapter shows that the new version of the sniffer is fully operational and its sensitivity is of the order of 10^{-6} ML .

3.4. Desorption of xenon from Ag(100)

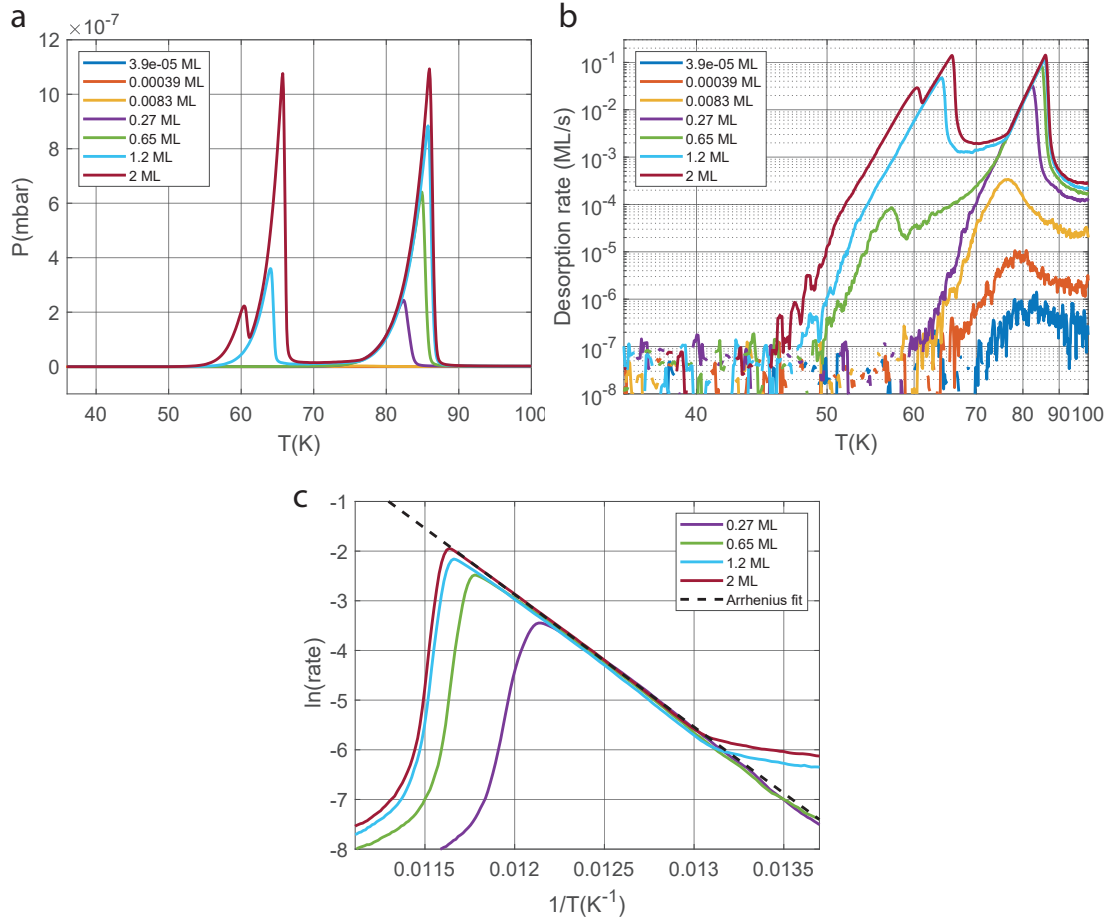


Figure 3.8 – a) and b) Temperature desorption spectra of xenon from Ag(100) for different coverages respectively on a linear and a logarithm scale. In figure 3.8b the x-axis shows T in a non linear scale. c) Arrhenius plot of the first layer peak. The Arrhenius fit (dashed line) is obtained fitting the data of the highest exposure.

4 Detection of Fe adatom exchange on Ag(100) by TDS investigation

According to DFT calculations of the catalytic activity of Fe₇ on MgO in the ammonia synthesis [11], which motivate this project, we will grow MgO on Ag(100) and then deposit Fe to obtain Fe clusters by thermal ripening. Many investigations of MgO growth on Ag(100) showed that the MgO morphology is not a flat and uniform layer but is constituted of MgO islands in the case of submonolayer coverage [40, 41]. The results presented for MgO grown on Ag(100) confirm this aspect. On the other hand, covering the substrate with a thick layer of MgO is possible but in this case the STM characterization is impossible. Therefore, on a typical sample accessible for STM studies, MgO islands coexist with bare Ag regions. Thus, it is expected that a sample prepared with Fe deposited on MgO/Ag(100) has areas where Fe is adsorbed on the bare Ag surface. For this reason, we first investigated the desorption of nitrogen from Fe on Ag(100).

Surface exchange mechanism generally involve metal atoms on a crystal surface. It designates the exchange of an adatom with an atom from the first layer of the substrate. This process has been studied in the past decades and is fundamental in the understanding of various surface mechanisms such as diffusion, epitaxial growth or subsurface alloying. Many experimental techniques of surface science were used for its investigation, including atom probe [42], field ion microscopy [43], photoemission spectroscopy [44–46], STM [47, 48], low energy ion scattering [49]. In this chapter, we present desorption spectra that highlight the existence of an exchange process between Fe adatoms and Ag atoms from the crystal surface. In addition to TDS, an STM investigation has been carried out to compare the morphology before and after the exchange takes place.

The surface energy calculated by full charge density (FCD) [50] gives 0.653 eV/atom for Ag(100) and 1.265 eV/atom for Fe(100). From a thermodynamic point of view, it is therefore expected that Fe atom integrates the surface of Ag(100) to minimize the total energy.

4.1 Desorption of N₂ from Fe/Ag(100)

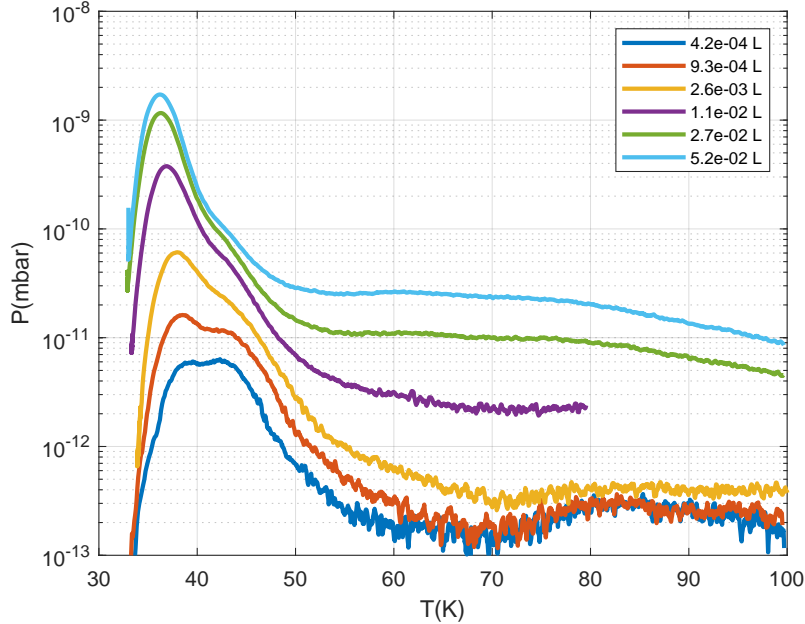


Figure 4.1 – TDS of ¹⁵N₂ adsorbed on clean Ag(100) for various exposures with a heating rate of 0.5 K/s.

We desorb isotopic ¹⁵N₂ from clean Ag(100) to obtain a TDS reference without interactions with other species at the surface. Isotopic ¹⁵N₂ ($m = 30$ amu) is used instead of natural nitrogen ($m = 28$ amu) to avoid interference with signals from desorbing CO ($m = 28$ amu). The sample is prepared according to our standard cleaning procedure. The surface morphology is characterized by STM. We obtain large atomically flat terraces with a typical width of a few hundreds of nanometers separated by monoatomic steps. After the preparation, the sample is cooled down to the lowest temperature the manipulator can reach using liquid helium in the flux cryostat, about 35 K. Exposure of the sample to ¹⁵N₂ and temperature programmed desorption are performed with the sniffer. We use one of the pulsed electrovalves to expose the sample to a controlled amount of nitrogen according to the description of the sniffer in chapter 3.3. Figure 4.1 shows the desorption spectra of isotopic N₂ from clean Ag(100) obtained for various initial exposures ranging from 0.00042 L up to 0.052 L. The heating rate is 0.5 K/s. We identify two peaks at 37 K and 43 K respectively. At the lowest exposure (0.00042 L), both peaks are nearly equal in intensity. When increasing the exposure, the first peak grows and the second becomes hidden by the first. Despite the absence of measurements at lower coverage, it is reasonable to identify the first peak with the desorption of ¹⁵N₂ from Ag(100) terraces and the second from the steps. Indeed, it is admitted that during the adsorption process, the adsorbed molecules decorate first kinks and steps, where the gas is more tightly bound, and then the terraces. This phenomenon was especially observed with

4.1. Desorption of N₂ from Fe/Ag(100)

rare gases [38,51]. Note that the first desorption peak starts at the very beginning of the TDS, and the initial desorption rate, that is proportional to the pressure, increases with higher exposure. This shows that the adsorbed nitrogen starts to desorb immediately after the exposure. The fact that desorption takes place at the lowest temperature our manipulator can reach does not allow a quantitative analysis of the desorption of nitrogen from Ag(100).

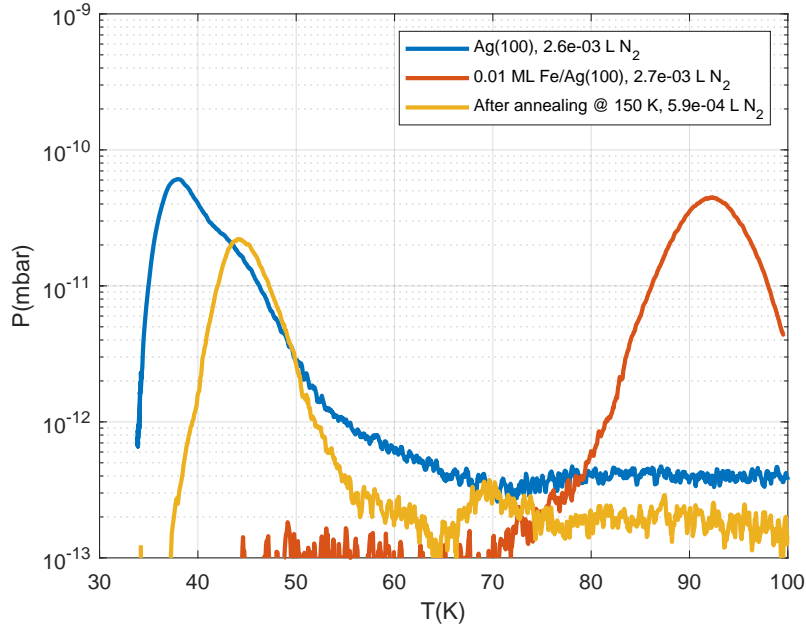


Figure 4.2 – TDS of ¹⁵N₂ from Ag(100) (blue), 0.01 ML Fe/Ag(100) (red), and annealed (yellow). The nitrogen exposure is about 10⁻³ L. Heating rate: 0.5 K/s.

About 0.01 ML of Fe is deposited on Ag(100) in order to observe its influence on the nitrogen desorption spectra. The monolayer is defined here as one Fe atom by Ag surface atom. The flux of Fe atoms is generated by sublimation of an iron rod with an e-beam evaporator. The temperature of the substrate during the evaporation is 40 K. After calibration by STM, the flux is determined to be $2 \cdot 10^{-3}$ ML/s and the total coverage deposited is 0.01 ML. A new set of TDS with the Fe/Ag(100) sample is performed following the same procedure for the exposure and the desorption as in the case of clean Ag(100). Figures 4.2 and 4.3 show several desorption spectra for exposures, respectively, 0.002 L and 0.02 L, that we refer to as low and high exposure. Each graph compiles TDS performed with similar exposure once on the clean Ag(100) surface (blue line), once after deposition of Fe as described above (red line), and finally after annealing of the Fe/Ag(100) surface (yellow line). For both, low and high exposure, the desorption spectra present significant changes. For low ¹⁵N₂ exposure, Fe deposition leads to the disappearance of the Ag(100) peak and to the appearance of a new one at about 92 K. This observation is interpreted as follow : the presence of Fe adatoms at the surface

Chapter 4. Detection of Fe adatom exchange on Ag(100) by TDS investigation

creates new adsorption sites for nitrogen molecules with a higher adsorption energy than the adsorption sites on bare silver. The adsorbed $^{15}\text{N}_2$ molecules diffuse on the Fe/Ag(100) surface and come to rest when they find a site with a high enough adsorption energy. The absence of the peak around 40 K demonstrates that no nitrogen molecules desorb from Ag(100) and that the quantity of nitrogen is low enough for all the molecules to be attached to Fe sites from where these desorb.

For high $^{15}\text{N}_2$ exposure, the desorption spectra of Fe/Ag(100) surface present two additional peaks to the one at 92 K, namely one at 40 K and one at 62 K, that we attribute to the desorption of nitrogen from silver and from a secondary Fe adsorption site. The interpretation is that the first Fe site is saturated because of the higher quantity of adsorbed nitrogen. So the $^{15}\text{N}_2$ molecules adsorb on the second site, that has a slightly lower adsorption energy, and finally on the silver sites that have lowest adsorption energy. Annealing of the Fe/Ag(100) sample to 150 K leads for both N_2 exposures to the disappearance of the peaks attributed to the Fe sites and only a peak around 40 K remains. This result suggests that after annealing there are no more Fe adatoms on the surface. This result is in perfect agreement with Langelaar and Boerma [49] who found that Fe adatoms on Ag(100) exchange with Ag atoms from the first layer in the temperature range of 130-150 K. Their conclusions are based on LEIS-TOF measurements. They observe that the Ar ion yield from Fe adatoms on Ag(100) decreases for a temperature increase from 130 K to 150 K. At the same time, the Ag adatom yield increases. Our observation is another evidence that this exchange between Fe and Ag atoms takes place.

In the next measurements, an extra 0.01 ML of Fe is deposited on the same sample after Fe/Ag site exchange. TDS measurements shown in figure 4.4 are performed with equivalent exposures and they are presented in chronological order. The sample is annealed after the end of each TDS as explained in the figure caption, such that the effect of annealing is visible in the next desorption spectrum. First, as expected the peaks attributed to Fe sites at 62 K and 92 K reappear, because the Fe deposition creates new Fe adatoms. Second, we observe a depletion of those peaks that is not correlated with the small variations of exposure. In particular, the decrease of the 92 K peak follows the chronological order of the measurements. This peak gradually decreases from TDS 1 to 4 that are followed by an annealing at 120 K. The decrease is much stronger between TDS 5 and 6 where the annealing increased to 130 K. Finally, after the annealing at 140 K, the Fe peak disappears completely.

First, these observations demonstrate the reproducible disappearance and reappearance of the Fe related peaks. They further show the effect of the annealing temperature. The first appreciable difference appears upon annealing at 130 K, with exchange seems completed at 140 K. Assuming an attempt frequency of $\nu_0 = 1 \cdot 10^{12} \text{ s}^{-1}$, the exchange process has an activation barrier of $0.33 \pm 0.03 \text{ eV}$. The 62 K peak has a different evolution: the intensity is not in agreement with the chronological order, but it disappears after the annealing at 140 K confirming that the peak is related to the presence of Fe adatoms.

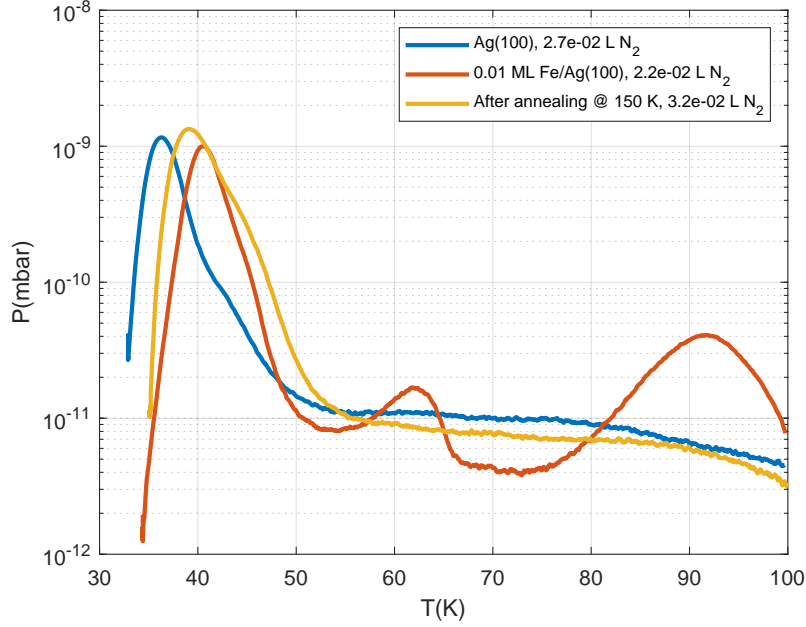


Figure 4.3 – Comparison of TDS of $^{15}\text{N}_2$ from Ag(100) (blue), 0.01 ML Fe/Ag(100) (red), and annealed to 150 K (yellow). The nitrogen exposure is in all cases close to 10^{-2} L. Heating rate: 0.5 K/s.

4.2 STM topography

An STM investigation is performed in order to observe the modification of the morphology induced by the exchange of Fe adatoms with Ag atoms. The Fe deposition is performed in the same conditions than in the previous part. After deposition, the sample is stabilized at 50 K with the STM head lowered onto the ramp for about 2 hours. This delay is required to thermalize the STM head and thereby to reduce the thermal drift during the image acquisition. Figure 4.5a shows the sample after deposition of Fe on Ag(100). The coverage is estimated by counting the objects at the surface. Most of the objects visible on the surface have a similar appearance like the one noted by A. The histogram of the apparent heights of the objects (figure 4.5c) confirms the narrow distribution in height centered at about 1.1 Å. This result shows that the deposited Fe adatoms on Ag(100) do not diffuse at 50 K which is in agreement with Langelaar and Boerma [49]. A second peak in the height distribution is visible at 0.5 Å, corresponding to objects like the one noted C. They could correspond to hydrogenated Fe atoms. The reduction of the apparent height of adatoms is a typical effect of the contamination with hydrogen. This effect was especially observed with Ti on h-BN/Rh(111) [52], with Co on Pt(111) [53], and with Co on graphene/Pt(111) [54]. Hydrogenation of reactive atoms like Fe is expected in a UHV chamber where the sample is exposed to the residual hydrogen partial pressure for a long time.

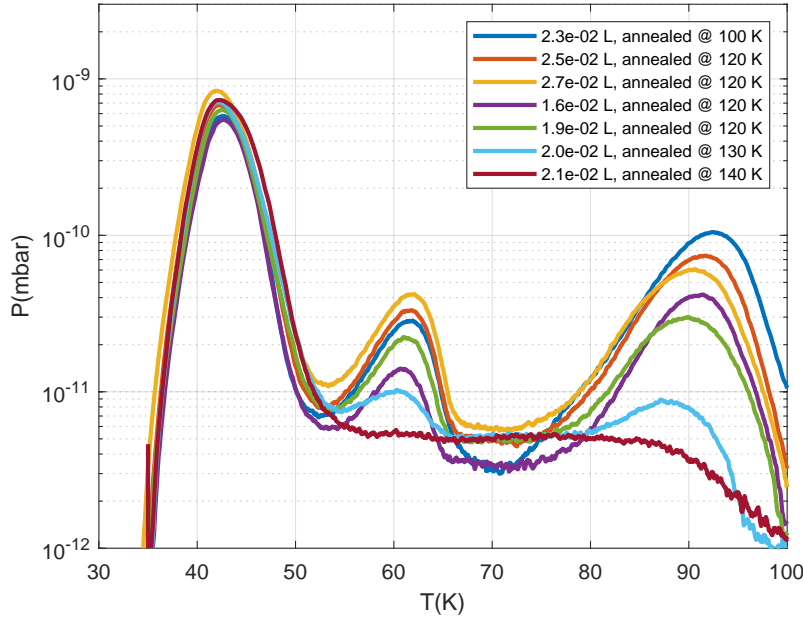


Figure 4.4 – TDS of $^{15}\text{N}_2$ after the second deposition of 0.01 ML of Fe on Ag(100). The order given in the legend follows the chronological order. The annealing temperature in the legend indicates the maximum temperature of the previous temperature ramp.

Figure 4.5b shows the morphology of the sample after annealing at 150 K. The apparent height histogram (figure 4.5d) is much broader. The majority of the objects have an apparent height of around 0.75 Å. They are supposed to correspond to Ag atoms from the surface that replaced the Fe adatoms after the exchange. Note the presence of larger objects on the surface. They might result from the diffusion of part of the Ag atoms on the surface. This would explain the reduction of the number of objects at the surface : the evaluation by counting gives 0.0094 ML before the exchange, and 0.0052 ML after (statistics on 457 and 626 objects respectively).

4.3 Conclusion

TDS investigation of nitrogen desorption from Fe adatoms on Ag(100) shows the capability of this technique to detect the Fe/Ag exchange process described in the literature. STM measurements show that the Fe species from which N_2 desorbs are isolated adatoms. These further detect exchange by the presence of a new surface species with significantly different apparent height. It must be noted that our interpretation of the measurements shown here does not explain all the involved processes. Technical limitations are an obstacle for a better comprehension: the desorption peaks observed at around 40 K are highly sensitive to the actual sample temperature and therefore to the temperature reading fluctuations. The reference junction of the thermocouple, that is placed in a

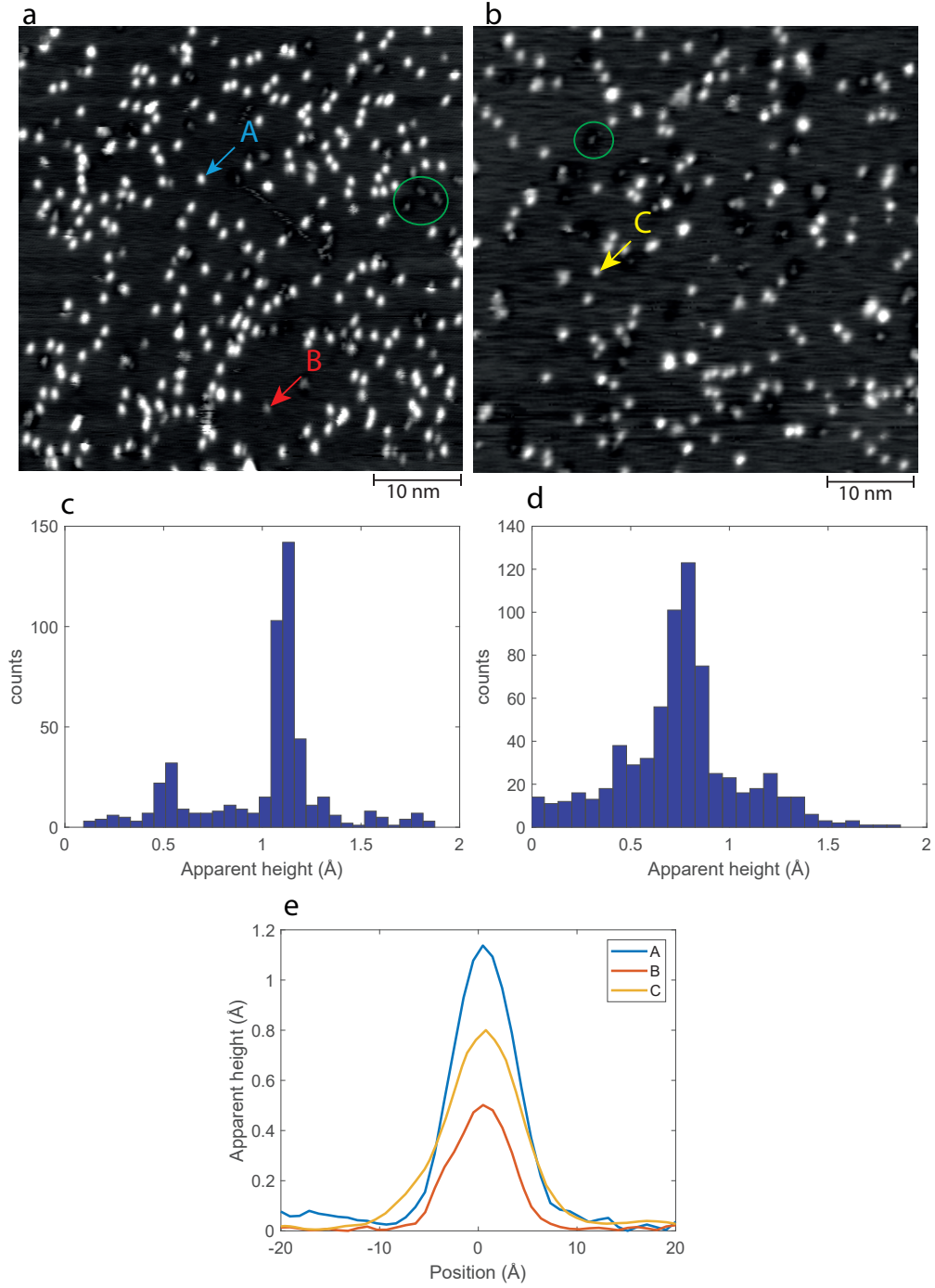


Figure 4.5 – a) and b) STM image of the sample with 0.01 ML Fe on Ag(100), respectively, before and after annealing at 150K. STM images are acquired at $T = 50$ K, $I = 1$ nA, $V = 1$ V. Objects A, B, and C are identified to be respectively Fe adatoms, Ag adatoms after exchange with Fe adatoms, and hydrogenated Fe adatoms. Objects encircled in green are supposed to be adsorbed CO molecules from residual gas. c) and d) Apparent height histogram of the objects visible in the STM images of Fe/Ag(100) before and after annealing at 150K. (e) Line profile of objects labeled A, B, and C.

Chapter 4. Detection of Fe adatom exchange on Ag(100) by TDS investigation

thermally regulated box, is submitted to very small temperature oscillations due to this regulation which imply variations in the thermocouple voltage at a constant sample temperature. Fluctuations of several degrees can be observed over a few hours when the sample is in the 40 K range. This can explain the different positions of the Ag peak in figure 4.3 showing desorption spectra which were measured at intervals of several hours. Another unknown parameter is the contamination of Fe atoms over the multiple exposure and desorption cycles. We have assumed that the N₂ adsorption does not change the adsorption and desorption properties of the sample.

5 Fe clusters on MgO/Ag(100)

Metal clusters on oxide thin films are widely studied as a model system for heterogeneous catalysis [55–62]. In particular, MgO films have been used in many heterogeneous catalysis experiments on surfaces [63–65]. Elementary processes such as electron transfer between substrate and supported atoms have been studied for MgO thin films [66, 67].

Ammonia catalysis with Fe₇ clusters has been investigated by Sljivancanin *et al.* [11]. They simulated by density-functional theory (DFT) such a cluster on an MgO surface. The calculations claim a molecular chemisorption state for N₂ with relatively high binding energy, thus suggesting that ammonia synthesis on these clusters might take place in a way similar to the biological enzyme nitrogenase. Inspired by these calculations we set out to investigate the Fe₇/MgO(100) system experimentally. The first step is to grow Fe clusters by thermal ripening on MgO/Ag(100).

A critical point in a catalysis experiment involving self-assembled metal clusters on MgO/Ag(100) is that this substrate does not provide any template to control the spatial order and cluster growth. On this type of surface, nucleation is therefore governed by the mean-field nucleation theory [68] applied to a homogeneous substrate if the surface is sufficiently smooth and defectless. In fact, defects can influence the nucleation and growth process, and dominate if they are present in high density [69, 70]. MgO thin films are characterized by the presence of different thicknesses and of island edges, and obtaining large and smooth patches still represents a challenge. Although largely investigated, MgO growth is still challenging and not completely mastered. The results found in the literature report typical island sizes that do not exceed a few tens of nanometers [40, 41, 71].

5.1 MgO growth on Ag(100): an STM characterization

5.1.1 dI/dV spectroscopy

For insulating oxide thin films, the apparent height in STM images does not reflect the topographic height and therefore other ways have to be explored to attribute an oxide film thickness to an island or terrace seen by STM. Figure 5.1a shows an STM image with a total MgO coverage of 47% ML where clean Ag(100), 1 ML, and 2 ML MgO areas coexist. Without additional information it is impossible to identify the areas in that image where there are islands of 1 and 2 ML MgO embedded in multiple terraces of Ag(100), and the respective apparent heights are in some cases the same. A technique combining force and current measurements with scanning probe to give high spatial resolution maps of the local three-dimensional insulator structure was proposed by Baumann *et al.* [72]. Nevertheless, this method implies to have a combined STM and AFM setup. Since we have only STM available, we decided to use dI/dV spectroscopy [73] to identify the MgO thickness. In this mode, the tip is placed above the region of interest with the feedback loop activated and the dI/dV signal is acquired by means of a lock-in amplifier. The bias is modulated with a frequency higher than the bandwidth of the STM feedback loop, typically about 1 kHz, so this additional signal does not influence the constant current measurement, and varies over the voltage range of interest which is typically several volts wide.

Figure 5.1c shows the dI/dV spectra obtained on Ag(100), 1 ML MgO and 2 ML MgO. The spectra obtained on MgO present two peaks separated respectively by 0.77 V on 1 ML MgO, and 0.47 V on 2 ML MgO. This result is in perfect agreement with the spectra reported by Fernandes *et al.* [74]. The dI/dV signal can be recorded in parallel with the STM topography to map it, and used to create a dI/dV map on which the morphology of the MgO islands can be clearly recognized. This image allows to identify the local thickness according to the amplitude of the lock-in signal. The images shown in figures 5.1a and 5.1b are a typical example of such a simultaneous recording. The measurement is performed at a bias of 2.4 V which gives the maximum contrast between the three different regions according to the spectra shown in 5.1c.

dI/dV spectroscopy associated with its imaging implementation is an efficient way to evaluate the total thickness and the quality of ultrathin MgO thin films grown epitaxially on Ag(100).

5.1.2 MgO morphology

The MgO growth consists in evaporating Mg on Ag(100) and in an O₂ background. The temperature of the evaporator T_{Mg} controls the Mg flux, the one of the substrate T_{dep} controls the Mg sticking coefficient, the rate of O₂ dissociation, and of formation of MgO,

5.1. MgO growth on Ag(100): an STM characterization

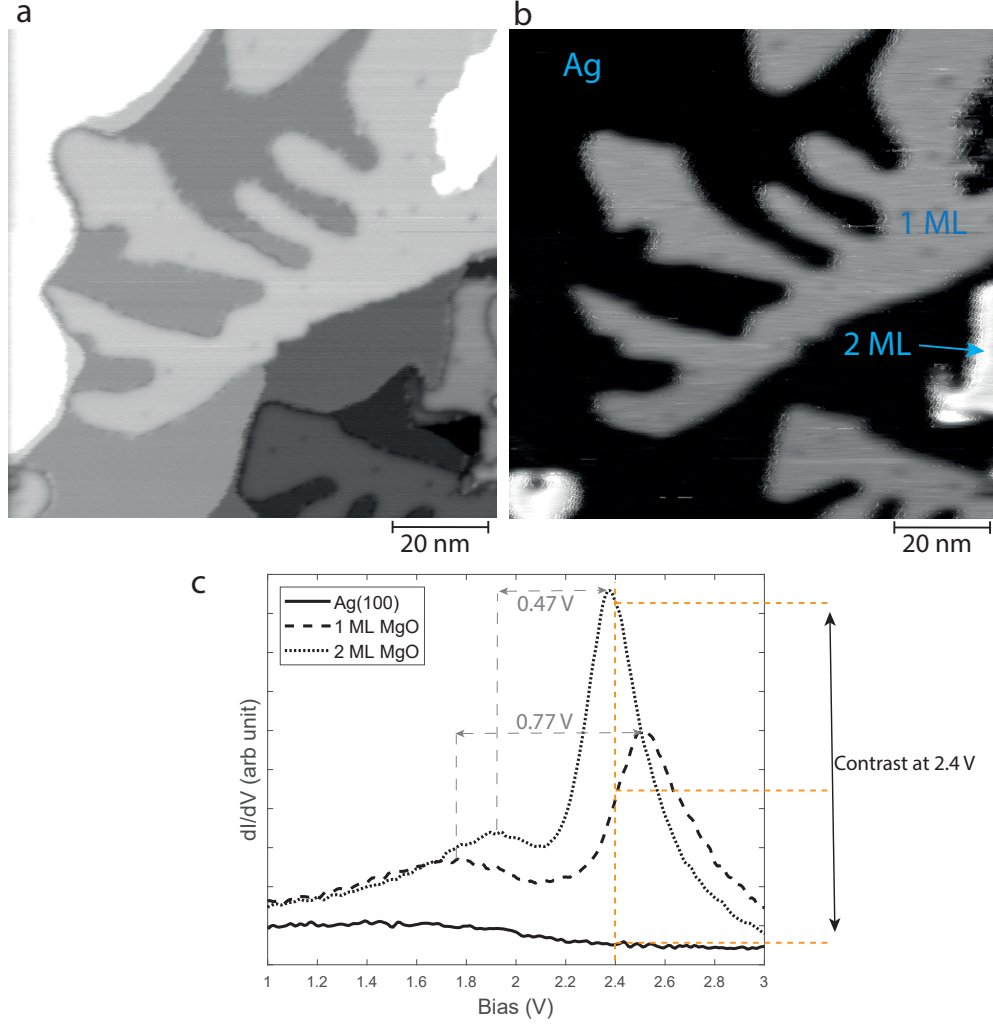


Figure 5.1 – a) STM image of MgO/Ag(100), $V = 2.4$ V, $I = 100$ pA. b) dI/dV image obtained from the lock-in signal. c) dI/dV spectra obtained for Ag(100), 1 ML MgO and 2 ML MgO.

and finally the cooling rate after growth defines how much time is left for the system in order to reach the minimum energy configuration. The coverage is determined by the exposure time. The sample is prepared with a sub-monolayer coverage, typically about 0.5 ML, where 1 ML MgO is defined as one MgO(100) unit cell per Ag(100) unit cell. The exposure time is adapted considering that higher T_{Mg} gives higher flux, and higher T_{dep} reduces the sticking coefficient. Different MgO growth recipes are tested in order to obtain smooth and large MgO islands. After all MgO growths, the sample is slowly cooled at a temperature rate of 0.2 K/s. The effect of cooling rate is not investigated in this work but it has been shown that a slow cooling can extend the MgO island size [75]. The global morphology is characterized by STM and the identification of the local MgO thickness (0, 1, 2 ML) is performed with dI/dV spectroscopy as described in the previous

section.

Figure 5.2 shows the typical morphologies of MgO patches we obtain. One of the difficulties is the lack of reproducibility. Figures 5.2a and 5.2b show two samples grown with the same parameters. In the first case, we observe smooth and well defined square island, and in the second, the MgO patches present lots of black dots that we identify as defects. Such point defects on 1 ML MgO have been reported by Fernandes *et al.* [74]. Figure 5.2c shows MgO patches with dendritic shape. This morphology is obtained with a lower flux and substrate temperature compared to figures 5.2a and 5.2b. The Ag(100) regions between the MgO patches are flatter than on the other samples shown on the same figure. This can be attributed to the low mobility of Ag atoms at $T_{\text{dep}} = 750$ K. Figure 5.2d shows another morphology with a too high substrate temperature: the MgO patches keep the general square shape but the internal composition of the patch consists of silver, 1 ML and 2 ML MgO that grow from a central seed and form a "flower-like" shape. Similar protrusions are also visible on figure 5.2a. These protrusions are several ML high and frequently cause STM tip instabilities due to the following effect. They present steep uprising steps, where the tip has to retract fast enough when approaching them with the given scan speed. The bandwidth of the feedback loop being finite, this retraction speed sometimes is insufficient and the tip touches the Ag protrusion whereby it changes its shape, often towards a more blunt tip apex.

For the investigation of the Fe cluster growth in the next part: we grew the MgO thin films at $T_{\text{Mg}} = 275^\circ\text{C}$ and $T_{\text{dep}} = 800$ K. The resulting MgO morphology has not the ideal square shape island, but the patches were smooth enough to be imaged by STM without tip crash.

5.2 Thermal ripening of Fe clusters on MgO/Ag(100)

The study of the growth of iron clusters has been carried out as follows: first of all, we determined the onset temperature of diffusion for Fe adatoms on 1 ML MgO. To do this, we deposit a small amount of Fe, typically less than 0.01 ML, on an MgO/Ag(100) sample at 40 K. The coverage is determined by counting the objects visible on 1 ML MgO on the STM images (figure 5.3a) and 1 ML Fe is defined as one Fe atom per Ag atom of the surface. Most of the protrusions have the same appearance, so we deduce that the objects on 1 ML are mostly Fe monomers. The sample is then annealed at a given temperature T_{anneal} and the surface is characterized by STM. The morphologies obtained for different temperatures T_{anneal} are compared. For $T_{\text{anneal}} < 250$ K, the surface is similar to the one shown on the image 5.3a. This observation allows us to conclude that Fe monomers are stable and do not diffuse up to 250 K on MgO/Ag(100). For annealing temperatures $T_{\text{anneal}} > 280$ K, there are no more monomers left on the surface, as shown on figure 5.3b. We observe instead larger protrusions, typically pinned at MgO defects. This can be explained by the small amount of Fe deposited, and therefore the high average distance

5.2. Thermal ripening of Fe clusters on MgO/Ag(100)

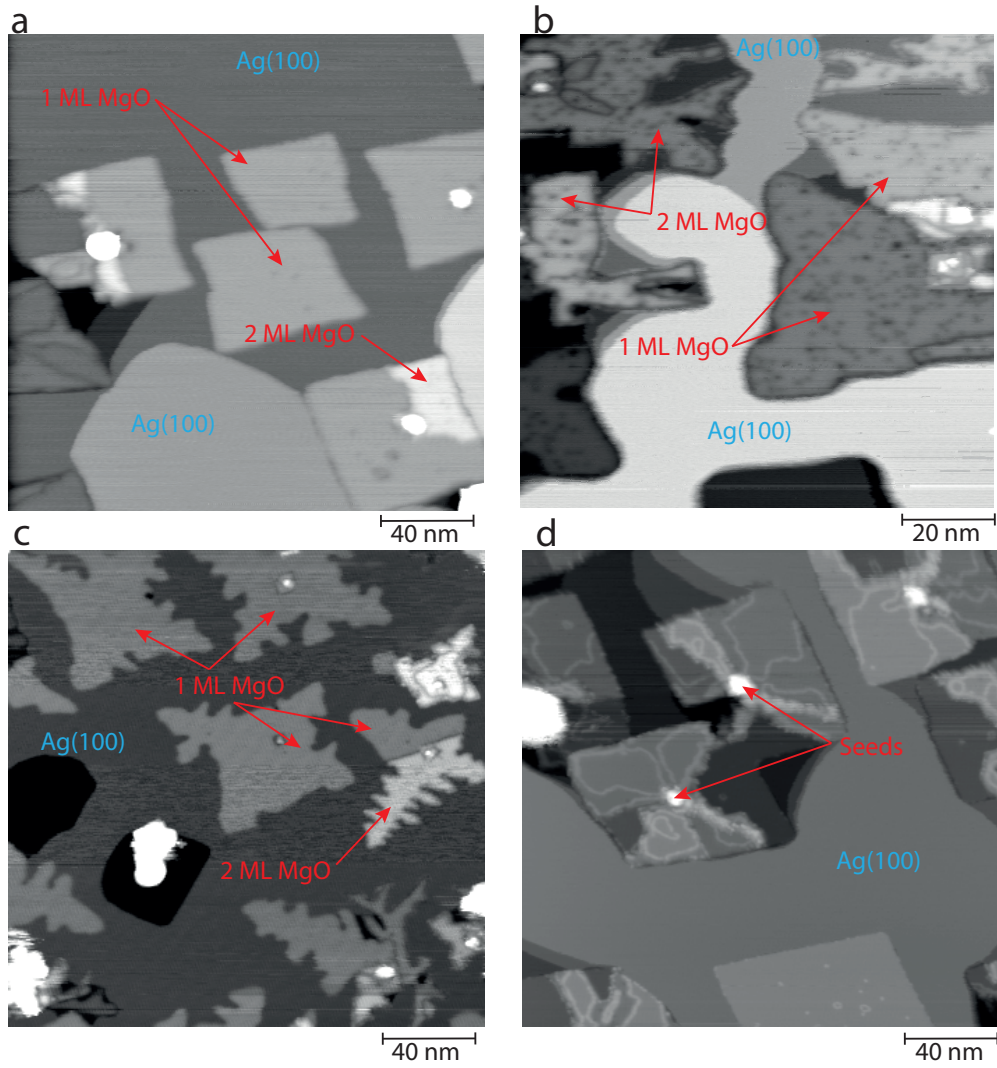


Figure 5.2 – STM topography of MgO/Ag(100) prepared with various temperatures of evaporation T_{Mg} and temperature of the substrate T_{dep} . Mg evaporation takes place under $1 \cdot 10^{-6}$ mbar O_2 . a) $T_{\text{Mg}} = 300^\circ\text{C}$, $T_{\text{dep}} = 790$ K. b) $T_{\text{Mg}} = 300^\circ\text{C}$, $T_{\text{dep}} = 790$ K. c) $T_{\text{Mg}} = 275^\circ\text{C}$, $T_{\text{dep}} = 750$ K. d) $T_{\text{Mg}} = 305^\circ\text{C}$, $T_{\text{dep}} = 813$ K. *STM parameters:* a) $V = 2.4$ V, $I = 100$ pA. b) $V = 2.4$ V, $I = 100$ pA. c) $V = 2.4$ V, $I = 100$ pA. d) $V = 2.4$ V, $I = 50$ pA.

between adatoms compared to the average distance between adatoms and defects or trapping centers. In this case, it is more probable that, while diffusing, an adatom reaches a defect site than another adatom.

Considering the present data, we conclude that the onset temperature for Fe adatom diffusion is between 250 K and 280 K.

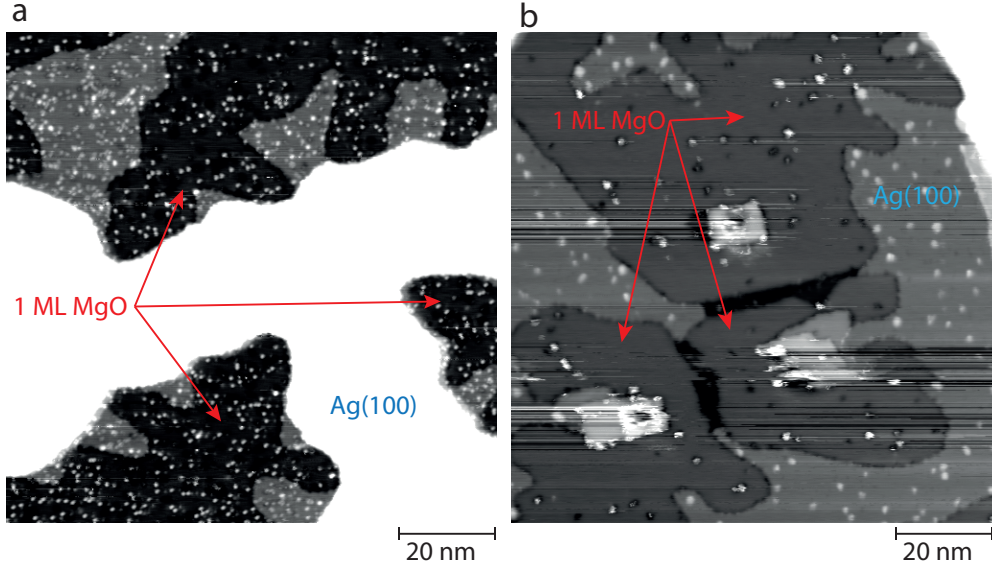


Figure 5.3 – a) 0.009 ML Fe on MgO/Ag(100), deposition at 40 K, measurement at 50 K. $I = 100$ pA, $V = -0.1$ V. b) 0.00038 ML Fe on MgO/Ag(100), deposition at 40 K, annealing at 310 K. $I = 100$ pA, $V = 0.1$ V. On both images the contrast is optimized to visualize the protrusions on MgO.

By increasing the amount of Fe, the morphology after annealing above the diffusion temperature changes significantly. Images 5.4a and 5.4b show the morphology for Fe coverage of $\theta_{\text{Fe}} = 0.054$ ML and $\theta_{\text{Fe}} = 0.072$ ML, respectively. In both cases, after annealing at 300 K, Fe clusters are present on MgO islands, suggesting nucleation after diffusion of Fe adatoms. The average size is estimated considering the Fe coverage and the density of Fe clusters visible on the surface. We obtain 11.7 ± 0.7 atoms per cluster for $\theta_{\text{Fe}} = 0.054$ ML and 12.1 ± 0.5 atoms per cluster for $\theta_{\text{Fe}} = 0.072$ ML. This similar size despite the difference in the amount of Fe deposited is explained by the lower cluster density in the first case. The presence of a second layer of MgO is also visible on both images. Its effect on nucleation is the following: small Fe clusters are visible along the step edges of the 2 ML island which acts as a nucleation site for the Fe adatoms. In addition, clusters visible on 2 ML MgO appear significantly larger and their density seems smaller than on 1 ML MgO.

We observe that Fe on MgO and Fe on Ag(100) have a very different growth morphologies. Figure 5.4c shows the profiles corresponding to the blue and red lines on the image 5.4a. It is clear that clusters on MgO have a 3D morphology. For Fe on Ag(100), the growth is

5.2. Thermal ripening of Fe clusters on MgO/Ag(100)

2D for the first layer but seems to be followed by 3D growth for the following layers which corresponds to the Stranski-Krastanov growth mode. The result is in perfect agreement with observations from Dézsi *et al.* [76] based on STM images. A more recent study performed by Canepa *et al.* [77] investigated the interdiffusion and segregation in the growth of Fe thin film (10 ML) on Ag(100), and revealed that intermixing by exchange process occurs at $T_{\text{dep}} < 250$ K. Considering this result and the Fe/Ag exchange process discussed in the previous chapter, Fe atoms deposited at 40 K and annealed at 300 K that are present on the Ag(100) regions should exchange with Ag atoms. Then, it seems likely that the islands at the surface are constituted of Ag atoms or a mixture of Ag and Fe atoms. This conclusion was not mentioned in Dézsi's work.

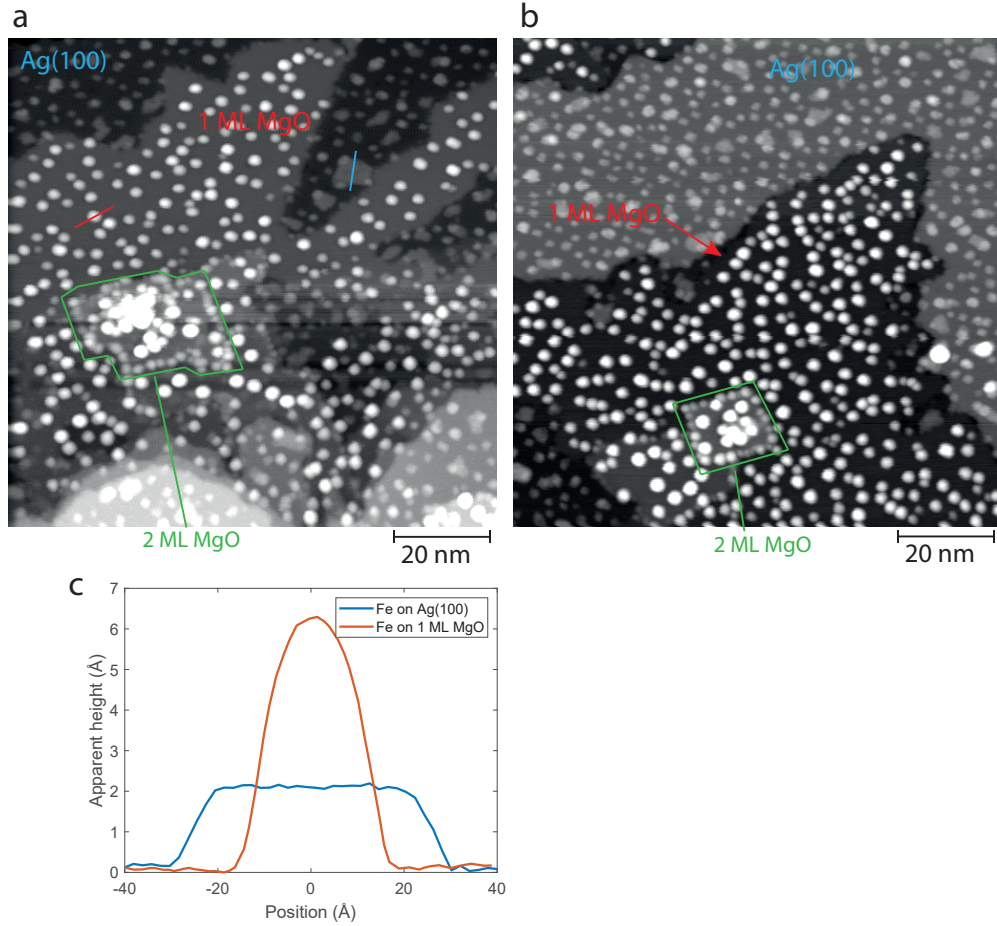


Figure 5.4 – a) $\theta_{\text{Fe}} = 0.054$ ML, $I = 100$ pA, $V = 2.4$ V. b) $\theta_{\text{Fe}} = 0.072$ ML, $I = 100$ pA, $V = 2.4$ V. In both cases $T_{\text{dep}} = 40$ K and $T_{\text{anneal}} = 300$ K. c) Profiles of the blue and red lines on image a).

5.3 N₂ on Fe clusters on MgO

After having obtained Fe clusters on MgO, the next step is to expose the sample to nitrogen and to perform TDS. The Fe clusters growth parameters are the ones shown in figure 5.4b. Note that, for TDS experiments, ideally the surface should be completely covered by MgO. However this is hardly compatible with STM characterization. As for the TDS of nitrogen on Fe/Ag(100) (chapter 4), the gas used is isotopic nitrogen ¹⁵N₂. The exposure procedure is as follows: The gas lines are pre-filled at a pressure of 10 mbar. The electrovalves are set in such a way that an average pressure of about 10⁻⁷ mbar is established in the desorption volume of the sniffer. After preparation, the sample is brought to 190 K and exposed to a dose of about 30 L.

Figure 5.5 shows the TDS realized between 190 K and 400 K with a ramp speed of 0.5 K/s. The choice of the initial and final ramp temperatures is motivated as follows: according to the DFT calculations [11], the Fe₇/MgO clusters with five pre-adsorbed N atoms can adsorb one molecule of nitrogen without dissociating it. The calculated binding energy for N₂ adsorption is 0.83 eV. Assuming that the desorption of N₂ molecules adsorbed on clusters is a first order process with a typical attempt frequency of $\nu_0 = 10^{13} \text{ s}^{-1}$, we estimate the corresponding desorption peak to be around 320 K. We decide then to cover the temperature range from 190 K to 400 K. Note that adsorption of N₂ with a desorption peak around 120 K [2] should be avoided by exposing the sample to N₂ at a sufficiently higher temperature, for instance 190 K.

The atomic masses 28 and 30 are recorded simultaneously in order to establish a correlation between the two signals. The first observation is that the signal of ¹⁵N₂ (30 amu) is almost flat over the whole temperature window. A small increase is to be noted between 300 and 350 K, where the pressure goes from $0.8 \cdot 10^{-11}$ mbar to $1 \cdot 10^{-11}$ mbar. However, this signal increase is perfectly correlated with the CO (28 amu) peak which is 2 orders of magnitude higher. Note that similar spectra are obtained for these two masses even without exposure to ¹⁵N₂. Therefore it seems likely that the increase in the signal background of mass 30 is an artifact due to CO desorption and does not correspond to a real nitrogen desorption. Alternatively, it could correspond to the desorption of ¹²C¹⁸O with mass 30 amu that have a natural abundance of 0.205%. This proportion matches the ratio between the two signals.

In conclusion, TDS measurements do not show molecular nitrogen desorption in the temperature range predicted by the DFT calculations. One explanation is that the used nitrogen exposure is much too low to passivate the Fe clusters. Indeed, according to the work carried out by Ertl *et al.* [2], it appears that the overall sticking coefficient σ_0 of the dissociative chemisorption of nitrogen on a clean Fe(111) surface is very small, about $2 \cdot 10^{-5}$ at 190 K (extrapolated to this temperature with $\sigma_0 = \nu_\sigma \exp(-E^*/RT)$, $\nu_\sigma = 2.2 \cdot 10^{-6}$ and $E^* = -0.8 \text{ kcal/mol}$). Assuming that the sticking coefficient for dissociative chemisorption of nitrogen on Fe cluster is similar than on Fe(111), it is clear

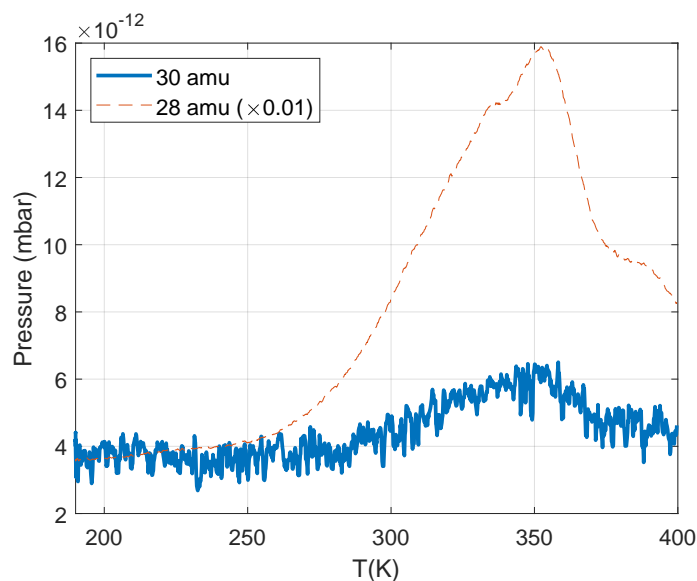


Figure 5.5 – TDS of $^{15}\text{N}_2$ (blue) on Fe clusters MgO/Ag(100). The signal of the mass 28 (red), corresponding to CO, measured in parallel is displayed to show the correlation between the 2 signals. The heating ramp rate is 0.5 K/s.

that the dose used in our experiment is by far insufficient to passivate the Fe clusters with chemisorbed nitrogen atoms as described in the DFT calculations (figure 1.4). The exposure required to expect a significant amount of dissociated nitrogen on the clusters would be of the order of 10^6 L, which is difficult to realize with our current procedure.

5.4 Conclusion

We studied the growth of MgO on Ag(100) by STM measurements combining topography and dI/dV mapping. We have identified growth parameters allowing us to obtain an appropriate surface as support for Fe adatoms and clusters.

The deposition of Fe adatoms on MgO/Ag(100) at 40 K followed by successive annealing allowed us to estimate the onset temperature for diffusion of Fe adatoms to be between 250 K and 280 K. Investigations by STM have shown that 3D Fe clusters are formed by thermal ripening with a sufficient Fe coverage. The cluster size estimated in our experiment is about 12 atoms per cluster for an Fe coverage in the range 0.05 - 0.07 ML.

Attempts to passivate Fe clusters and to adsorb undissociated nitrogen according to the process calculated by [11] were not conclusive. We presume that the too low nitrogen exposure during the experiment is at the origin of the absence of nitrogen desorption in our results.

Considering the experimental difficulties related both to the preparation and STM

Chapter 5. Fe clusters on MgO/Ag(100)

measurements of MgO thin films, as well as the weak control of the growth of the Fe clusters, we decided to move to another support, graphene/Ir(111), investigated in the next chapter. The choice of the new system is mainly motivated by two aspects :

- The presence of a template to better control the cluster size distribution and spatial order.
- The sample preparation must produce a surface smooth enough and completely covered to allow STM measurements without the difficulties encountered with MgO/Ag(100).

6 Fe clusters on graphene/Ir(111)

As described in the previous chapter, TDS from N_2 exposed Fe cluster on MgO shows evidence neither of molecular nor of atomic nitrogen. Furthermore, the investigation of the thermal ripening of Fe clusters on MgO presents a lot of technical difficulties that make this experiment hard to control. We decided to investigate a new system to self-assemble the clusters and to measure nitrogen adsorption and desorption. A few candidates for the crystal substrate and the decoupling layer, with the presence of a template to get a better control on the cluster size, have been considered: aluminum sulfide phases on Al(111) [78], ultrathin alumina films on Ni_3Al (111) [79,80], and graphene on Ir(111). Graphene/Ir(111) has the advantage to be easy to grow and it creates a long range superstructure called moiré, originating from the slightly different lattice parameters of the graphene layer and the Ir(111) surface. This system has been shown to be an excellent template to grow cluster superlattices [81].

We investigate first the growth of Fe clusters on graphene/Ir(111) and their stability as function of the temperature. In a second phase, we perform TDS of $^{15}N_2$ to characterize their ability to adsorb molecular nitrogen.

6.1 Graphene on Ir(111)

In our UHV environment, two methods of graphene preparation can be considered: thermally induced surface segregation and chemical vapor deposition (CVD). The segregation method is possible with substrates that contain carbon, like ruthenium [82] or carbides [83]. In our experiment we observed graphene patches formed by carbon segregation on Ir(111) after annealing of the crystal. The difficulties to control the parameters and to obtain exactly one monolayer make segregation a non optimal method according to our aim to have a homogeneous sample with a well defined cluster size. In order to avoid the presence on the surface of isolated graphene patches, the annealing procedure have been optimized to minimize the carbon segregation. CVD is a method

commonly used to grow graphene on Ir(111). This method consists in growing graphene by decomposing a hydrocarbon at the crystal surface. Graphene on Ir(111) grown by CVD has been characterized by N'Diaye *et al.* [81, 84]. The moiré periodicity is 25.2 Å and its unit cell can be approximated by a (10×10) graphene adlayer on a (9×9) Ir(111) slab (figure 6.1a).

We prepared the Ir(111) crystal with repeated cycles of Ar^+ sputtering (1500 eV, $3.1 \mu\text{A}/\text{cm}^2$, 300 K) and flash-annealing at 1450 K for 1 min, yielding clean terraces several tens of nanometer wide as verified by means of STM. Graphene is prepared in situ by CVD. For this, we expose the Ir(111) surface at 1400 K to $5 \cdot 10^{-7}$ mbar of ethylene (C_2H_4) for 100 seconds. The applied dose ensures saturation coverage of one full ML. The moiré pattern we obtain is shown in figure 6.1b. The moiré is imaged in the dark-atop contrast mode described by NDiaye *et al.* [84], *i.e.*, the atop regions described in figure 6.1a appear as dark depressions in a bright surrounding. The contrast is obtained with a low tunneling voltage ($V = 32$ mV in ref. [84], $V = 10$ mV in figure 6.1b). This contrast can be inverted (bright-atop contrast) when using high bias voltage ($V = 1.5$ V [84]).

The used recipe yields a completely covered surface. The preparation is reproducible and the characterization by STM does not present any experimental difficulties. As shown in the figure, the moiré provides a well ordered and homogeneous template for a long range order of clusters.

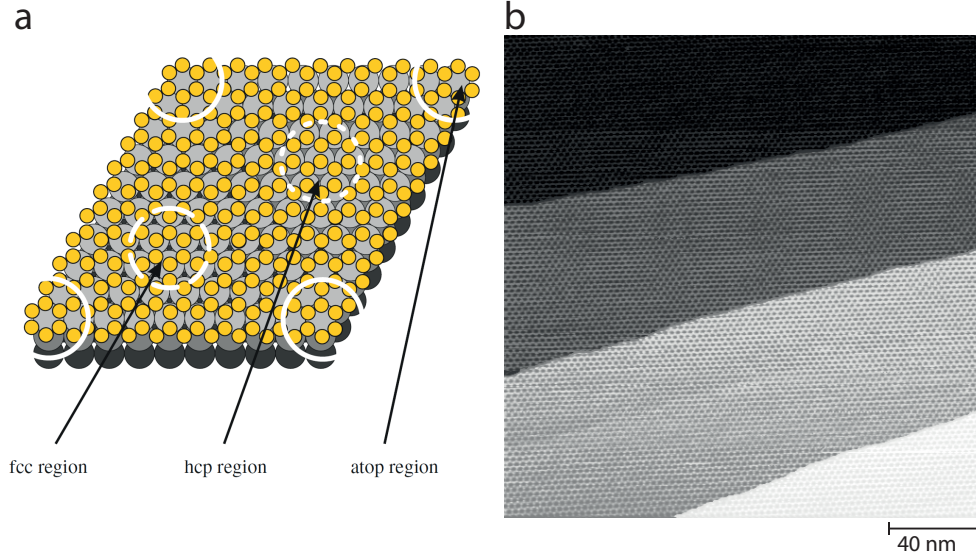


Figure 6.1 – a) Schematic illustration of the $\text{C}(10 \times 10)/\text{Ir}(9 \times 9)$ unit cell (Adapted from [84]). b) Graphene/Ir(111), $I = 3$ nA, $V = 10$ mV.

6.2 Growth and stability investigation of Fe clusters on graphene/Ir(111)

In this part, we present the investigation of the nucleation and of the stability of Fe clusters on graphene/Ir(111). The Fe deposition is performed by the e-beam evaporator present on the chamber described in chapter 2. The Fe flux is calibrated by STM. The procedure used in chapter 5 of counting the density of individual atoms cannot be used here as the Fe adatoms are mobile on graphene/Ir(111) at the lowest temperature the sample can reach in the He-flux manipulator. Details of the procedure of the calibration used here are shown in appendix A. The reference Fe flux used in the following depositions is determined to be 0.16 ML/min, where 1 ML corresponds to the surface atomic density of Ir(111).

Figure 6.2a shows an STM image of 0.1 ML Fe deposited on graphene/Ir(111) at $T_{\text{dep}} = 300$ K. The presence of only a few clusters on the surface indicates the absence of effect of the moiré pattern on the nucleation under those conditions. In agreement, N'Diaye *et al.* [85] report the absence of a cluster superlattice for Fe deposition at 300 K on graphene/Ir(111) (figure 6.2b). Note that in their case the cluster density is much higher than what we obtain which can be explained by the higher Fe coverage ($\theta_{\text{Fe}} = 0.77$ ML) and the higher flux, about 10^{-2} ML/s, a factor of 3 higher than the one we used. Nucleation of several metals on graphene/Ir(111) has been investigated [85]. The authors considered three criteria of the tested material favoring the formation of a superlattice. The cohesive energy, that indicates the possibility for a material to form strong bonds with its own. The matching with the lattice parameter of graphene/Ir(111) which is 2.452 Å. 2.7 Å is considered as the optimal nearest neighbor distance in the metal as the effective lattice parameter for small clusters is lower than the bulk value. The third factor they considered is the extension of a localized valence orbital of the tested metal. A large extension allows it to efficiently interact with the graphene π -bond.

They observed that materials with low cohesive energy such as Fe ($E_{\text{coh}} = 4.28$ eV) tend not to form cluster superlattices on the graphene moiré on Ir(111) at 300 K. The cohesive energy of the tested metals that form a cluster superlattice on graphene/Ir(111) (Ir, Pt and W) is in the range 6-8 eV. Furthermore, the lattice parameter of Fe is 2.483 Å whereas it is in the ideal 2.7 Å range for Ir, Pt and W. Also the valence d-orbital radius is much lower for Fe ($r_d = 38.2$ pm) than for Ir, Pt or W (65-80 pm). For the three factors used as a guideline, the Fe parameters indicate that it is not expected to form a superlattice on graphene/Ir(111), which is in agreement with experimental data. The corrugation of the binding energy of Fe on the graphene moiré is apparently too weak to trap the Fe adatoms in the moiré unit cell at 300 K. In the following, we will reduce the temperature of the sample to control the Fe nucleation.

In order to reduce the mobility of the Fe adatoms, the sample is cooled to a temperature of $T_{\text{dep}} = 50$ K for deposition. The sample is measured by STM after annealing at

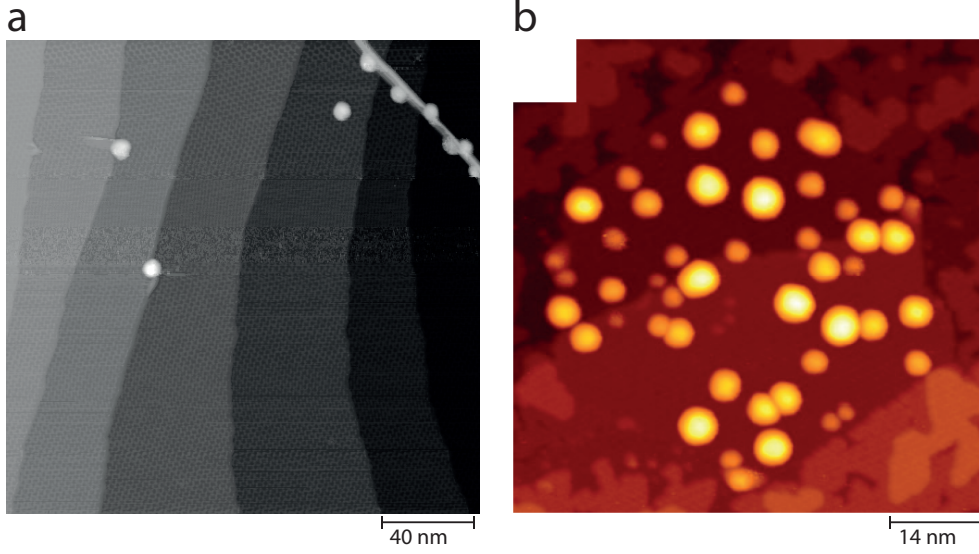


Figure 6.2 – a) STM image of 0.1 ML Fe on graphene/Ir(111), $T_{\text{dep}} = 300$ K. $V = 5$ mV, $I = 3$ nA. b) STM image of 0.77 ML Fe deposited at 300 K on a graphene/Ir(111) sample (adapted from [85]).

different temperature T_{anneal} . The results, which we will detail afterwards, are shown in figures 6.3 and 6.4 for Fe coverages of 0.3 ML and 0.4 ML, respectively. The first and main observation is the formation of an Fe cluster superlattice following the periodicity of the moiré. At low deposition temperature, the adatoms are trapped in the moiré cell where they can diffuse and form a single cluster with a size given by the amount of atoms falling into that moiré unit cell [12]. The second observation is that the long range order of the clusters decreases with increasing annealing temperature, and for 0.4 ML of Fe eventually disappears at $T_{\text{anneal}} = 600$ K (figure 6.4d), resulting in coalescence to larger clusters.

Clusters are classified in two categories: primary clusters, formed by the nucleation of Fe adatoms during deposition, and secondary clusters, resulting from Smoluchowski ripening, i.e., from the diffusion of primary clusters to a neighboring moiré unit cell where they coalesce with a neighboring cluster. One of the evidences that Smoluchowski ripening prevails instead of Ostwald ripening comes from the morphology of the primary and secondary clusters that are especially visible on the image 6.3b: the black areas, corresponding to one or more vacancies in the cluster superlattice, are always next to one or more clusters of larger apparent sizes that are the secondary clusters formed by the capture of the diffusing primary clusters. With Ostwald ripening, we would expect that the clusters next to an empty unit cell grow uniformly as they collect the same amount of material from the vanishing cluster. The mean size \bar{n}_1 of the primary clusters, calculated considering the nominal number of Fe adatoms deposited on the surface per moiré unit cell, is 26 for 0.3 ML and 35 for 0.4 ML (these numbers simply result from the

6.2. Growth and stability investigation of Fe clusters on graphene/Ir(111)

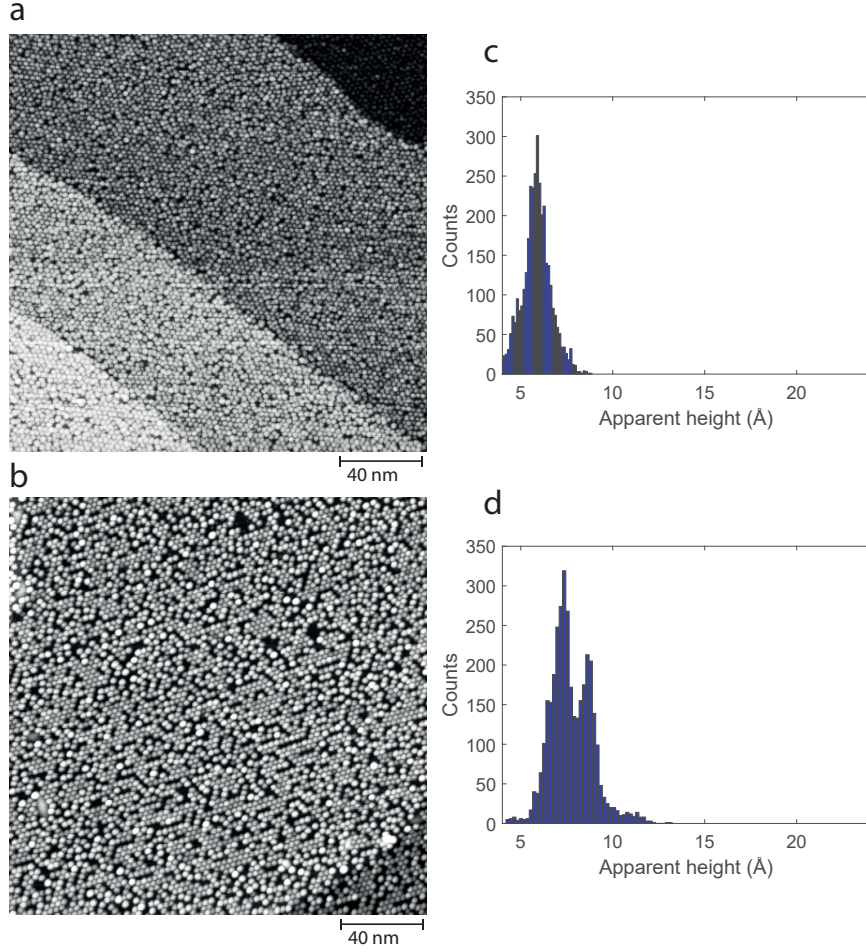


Figure 6.3 – a) and b): STM images of 0.3 ML Fe deposited on graphene/Ir(111) at 50 K, and measured at 50 K and 300 K, respectively. c) and d): apparent height distribution of the Fe clusters for STM images a) and b), respectively.

fact that the Fe coverage is calibrated with respect to the density of Ir surface atoms and that the moiré unit cell has 87 ± 3 atoms [84]). The secondary cluster average size \bar{n}_m can be expressed as a function of \bar{n}_1 : $\bar{n}_m = m \cdot \bar{n}_1$, where m is the number of captured primary clusters.

Note that the cluster size is calculated assuming the same sticking coefficient for Fe on graphene/Ir(111) and on bare Ir(111). It has been shown on related systems that the effective sticking coefficient is lower on the decoupling layer than on the metal substrate. Natterer *et al.* [86] obtain a sticking coefficient of $s_0 = 0.74$ for Mn on *h*-BN/Rh(111) at 10 K. Furthermore, Auwärter *et al.* [87] report a strong temperature dependence of the sticking probability of Co on *h*-BN/Ni(111). Should the sticking coefficient be smaller than one for deposition at 50 K in the present case, one needs to correct the cluster sizes accordingly.

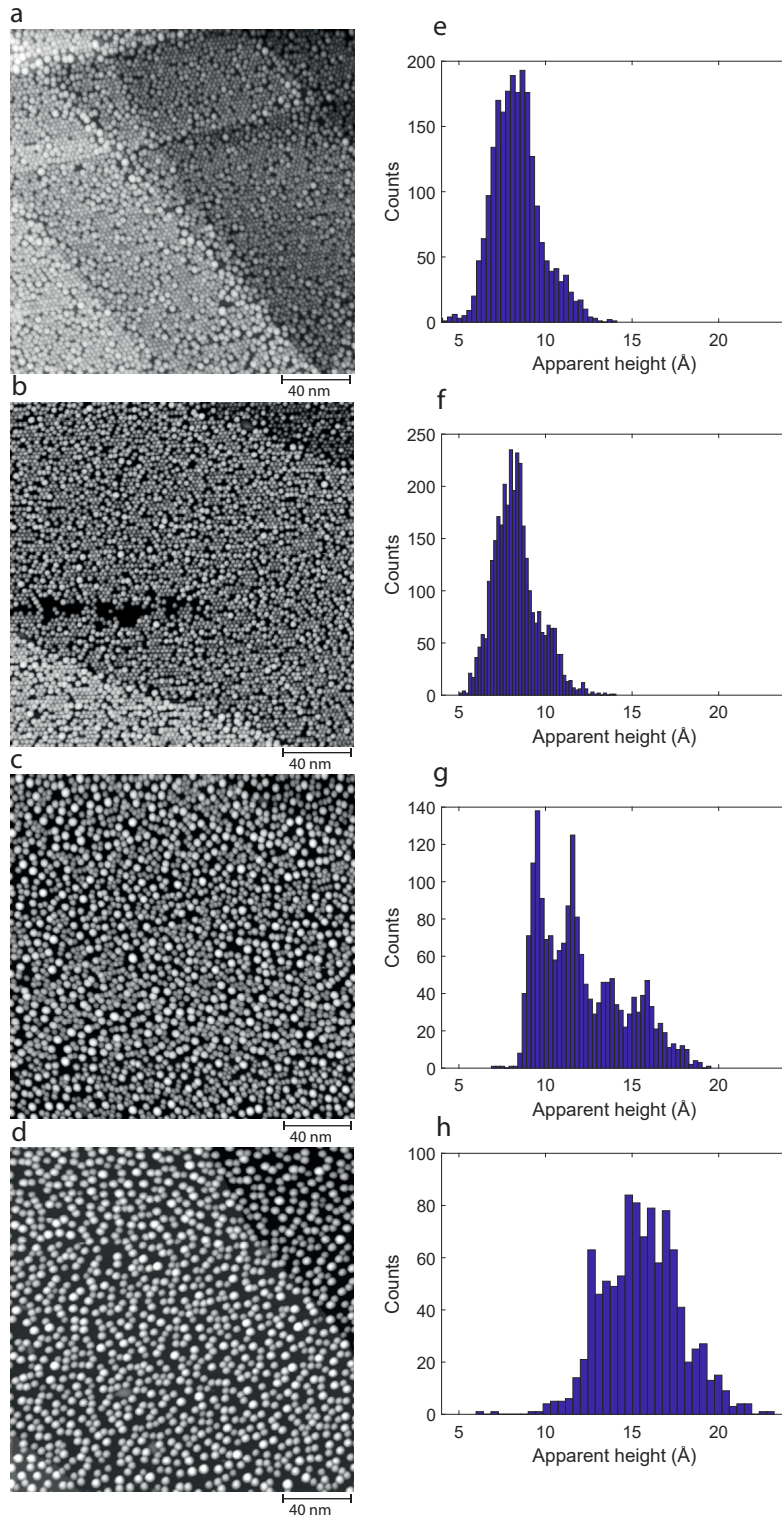


Figure 6.4 – a), b), c) and d): STM images of 0.4 ML Fe deposited on graphene/Ir(111) at 50 K and measured at 300 K after annealing at 300 K, 400 K, 500 K, and 600 K, respectively. e), f), g) and h): apparent height distribution of the Fe clusters for STM images a), b), c) and d), respectively.

6.2. Growth and stability investigation of Fe clusters on graphene/Ir(111)

For each sample, the apparent height of the clusters is represented in the histograms next to corresponding STM images in figures 6.3 and 6.4. It is determined relative to the height of the terrace on which the clusters are located. The consistency of the histogram thus depends on the ability of having a well defined reference, which is difficult when the surface is densely covered by clusters, like in figures 6.3a and 6.4a.

Deposition of 0.3 ML Fe on graphene/Ir(111), annealed and measured at T_{anneal} (figure 6.3a) shows that almost every moiré unit cell is occupied by an Fe cluster. The histogram of apparent heights on figure 6.3c does not allow to identify several distinct cluster sizes. Only one peak is present, centered at 6 Å. For $T_{\text{anneal}} = 300$ K (figure 6.3b), 37% of the moiré unit cells are empty because of the diffusion of a fraction of the primary clusters. Nevertheless, the majority of them are still present, as confirmed by the histogram on figure 6.3d. The first peak, centered at 7 Å corresponds to the primary clusters and is still dominant. A second peak, at about 9 Å, has appeared and is attributed to the Fe clusters corresponding to $m = 2$.

For 0.4 ML Fe, the sample is annealed at 300 K, 400 K, 500 K, and 600 K. The Fe cluster size distribution is in line with the evolution of STM images after successive annealing. At $T_{\text{anneal}} = 300$ K, the histogram (figure 6.4e) shows a peak centered at 8 Å, followed by a shoulder around 11 Å. At $T_{\text{anneal}} = 400$ K, the histogram (figure 6.4f) shows a significant increase in the number of objects around 11 Å with the appearance of a peak at this value. The first peak, centered at 8 Å, is attributed to primary clusters, and the second peak to secondary clusters corresponding to $m = 2$. This evolution is in agreement with the increase of the proportion of vacant sites, 30% and 39% for, respectively, $T_{\text{anneal}} = 300$ K and $T_{\text{anneal}} = 400$ K.

At $T_{\text{anneal}} = 500$ K, a majority of primary clusters has diffused, making the cluster superlattice almost disappear in figure 6.4c. The corresponding histogram in figure 6.4g shows four clearly distinguishable peaks. A large part of the primary clusters of apparent height smaller than 8 Å, still present at $T_{\text{anneal}} = 400$ K, diffused and formed secondary clusters of various sizes, $m = 2, 3$ and 4, corresponding to peaks centered, respectively, at 11 Å, 13 Å and 15 Å. Finally, at $T_{\text{anneal}} = 600$ K (figure 6.4f), all the primary clusters have diffused, as shown in the histogram in figure 6.4h. The peaks corresponding to clusters of size $m = 1$ and 2 have disappeared, leaving room for larger clusters with a less defined distribution. Note that the identification of peaks is not straightforward, and the assignments given here are only tentative.

The histograms of figure 6.4 highlight that at certain annealing temperatures certain cluster sizes disappear. This is an other evidence that the Smoluchowski ripening takes place, as there is no sign of a gradual disappearance of the clusters. Note that this argument was also pointed out by Gerber *et al.* [88] to establish that, upon CO exposure, Pt cluster ripening on graphene/Ir(111) proceeds by Smoluchowski ripening.

6.3 Nitrogen desorption from Fe clusters on graphene/Ir(111)

6.3.1 Adsorption and slow dissociation of $^{15}\text{N}_2$ on Fe clusters

In this part, we investigate the desorption of isotopic nitrogen $^{15}\text{N}_2$ adsorbed on 0.4 ML Fe on graphene/ Ir(111) sample prepared as described in the previous parts. Exposure of the sample to $^{15}\text{N}_2$ and temperature programmed desorption are performed with the sniffer. As in previous TDS experiments presented in this work, we use one of the pulsed electrovalves to expose the sample to a controlled amount of nitrogen. The sample is exposed at a temperature of $T_{\text{exp}} = 50$ K. TDS are realized between 50 K and 280 K with a temperature ramp of 1 K/s. In this temperature range, we can assume that the sample remains in a state similar to the one shown in figure 6.4a, exhibiting mostly primary clusters with a mean size of 35 atoms.

Nitrogen adsorption is linked to the presence of Fe clusters on graphene, as shown in figure 6.5a. The TDS on bare graphene with an $^{15}\text{N}_2$ exposure of 0.13 L shows no $^{15}\text{N}_2$ desorption, while a second one after deposition of 0.4 ML of Fe and exposure to 0.013 L shows a nitrogen desorption peak at around 120 K. Note that the dose of $^{15}\text{N}_2$ is ten times smaller in the case of Fe clusters and the desorption peak is prominent.

A series of TDS of $^{15}\text{N}_2$ adsorbed on 0.4 ML Fe on graphene/Ir(111) is realized with exposures from $1.5 \cdot 10^{-3}$ L to $1.4 \cdot 10^{-1}$ L (figure 6.5b). Two desorption peaks are observed: the one previously reported at around 120 K, and a second one that appears starting from an exposure of $8.5 \cdot 10^{-2}$ L, centered at about 92 K. The shape of both peaks is similar and suggests that they are first order desorption peaks.

Considering the low quantity of $^{15}\text{N}_2$ dosed, about 0.1 L even for the highest exposure, and the low sticking coefficient of N_2 on Fe(111) [2], the Fe clusters can only accommodate sub-monolayer of adsorbed N_2 . For comparison, the N_2 exposure required to barely saturate the first monolayer on a surface of Fe(111) is of the order of 10^2 L [2]. For the latter case, desorption parameters, deduced from a combination of AES and TDS, are $E_d = 0.33 \pm 0.05$ eV for the desorption energy at low coverage, and $\mu_0 \approx 2 \cdot 10^{10 \pm 1} \text{ s}^{-1}$ for the prefactor. In our case, the Redhead approximation of the desorption energy based on the temperature of the maximum desorption rate, and assuming a typical value for the prefactor of $\mu_0 = 10^{13} \text{ s}^{-1}$, yields $E_d = 0.32 \pm 0.05$ eV for the 120 K peak, and $E_d = 0.24 \pm 0.05$ eV for the 92 K peak. Note that the desorption energy for nitrogen on Fe(111) obtained by Ertl *et al.* [2] is close to the desorption energy estimated for the 120 K peak in figure 6.5a. Nevertheless, the maximum desorption rate of the TDS in ref. [2] is at about $T_p = 158$ K. This difference is due to the unusually small value of the prefactor measured in ref. [2]. The Redhead approximation of the 120 K and the 92 K peaks, assuming the value for the prefactor $\mu_1 \approx 2 \cdot 10^{10 \pm 1} \text{ s}^{-1}$, yields respectively 0.24 ± 0.02 eV and 0.19 ± 0.02 eV.

6.3. Nitrogen desorption from Fe clusters on graphene/Ir(111)

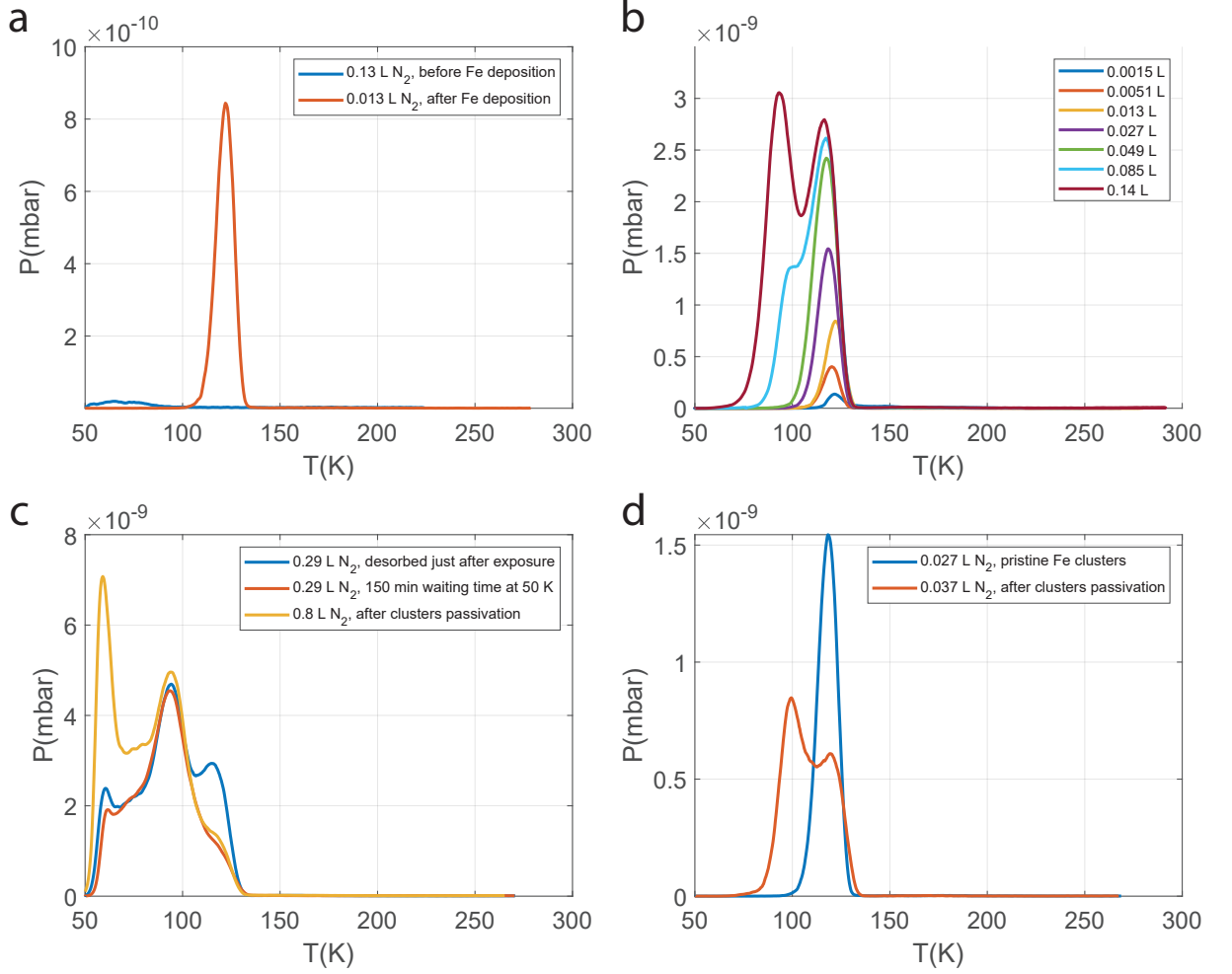


Figure 6.5 – a) TDS of $^{15}\text{N}_2$ before Fe deposition (blue), and after deposition of 0.4 ML Fe (red) on graphene/Ir(111). b) TDS of $^{15}\text{N}_2$ adsorbed on 0.4 ML Fe on graphene/Ir(111) with various exposures at 50 K. c) and d) TDS of $^{15}\text{N}_2$ adsorbed on 0.4 ML Fe on graphene/Ir(111) with various exposures at 50 K, performed before and after 150 min waiting time between exposure and TDS (details in text). The ramp speed is 1 K/s for all TDS.

The existence of multiple desorption peaks is not surprising considering that the Fe clusters on which the $^{15}\text{N}_2$ are adsorbed have a 3D structure that present multiple facet orientations, edges and kinks, which are potential adsorption sites with their specific desorption parameters.

Figure 6.5c shows a TDS with a slightly higher exposure of 0.29 L (blue spectrum). In addition to the two peaks described above, there is a third peak at about 60 K, and the adsorption sites corresponding to 92 K peak are saturated. In the next TDS, the same exposure is applied and desorbed after 150 min waiting time at 50 K (red spectrum in

figure 6.5c). The 120 K peak almost disappears and only a shoulder remains, whereas the 92 K peak remains unchanged. The 60 K peak is slightly depleted, which can be rationalized by the slow desorption rate of $^{15}\text{N}_2$ from the corresponding adsorption site at 50 K during the waiting time. After a re-exposure of 0.8 L on the same sample (yellow spectrum), the reduction of the 120 K peak is confirmed as well as the saturation of the 92 K peak. On the other hand, the 60 K peak increases.

The observed difference of the 120 K desorption peak before and after the waiting time suggests the disappearance of most of the corresponding adsorption sites. Our hypothesis, according to Ertl's observations [2], is that the $^{15}\text{N}_2$ molecules adsorbed on those sites slowly dissociate into ^{15}N atoms whose desorption is expected to take place at much higher temperature. For comparison, the desorption peak of dissociated ^{15}N on an Fe surface is around 900 K [89,90]. The Fe sites of our clusters that correspond to the 120 K peak are thus occupied by the dissociated ^{15}N which prevents the adsorption of new $^{15}\text{N}_2$ molecules on these sites. Figure 6.5d confirms the effect of the waiting time for TDS with much lower exposure ($\simeq 0.03$ L). The TDS taken directly after exposure has only the 120 K peak while after 150 min waiting time at 50 K, the 120 K peak is strongly reduced and the 92 K peak, shifted to around 100 K, is present.

Altogether, there are three adsorption sites for molecular nitrogen on 35 atom sized Fe clusters on graphene/Ir(111). The one with the highest binding energy is occupied first and is attributed to Fe facets of the clusters. The two other adsorption sites are possibly at the interface between Fe cluster and graphene or at an other site on the Fe cluster like kink or edge. One important discovery is the slow dissociation of molecular nitrogen at 50 K adsorbed on the highest energy site. The dissociated and atomically adsorbed N is so strongly bound that it blocks further N_2 adsorption and dissociation, very much as in the experiments on single crystal surfaces, and as in the real Haber-Bosch catalyst.

Since the slow dissociation mechanism of N_2 on Fe clusters allows to obtain clusters with adsorbed nitrogen atoms, it is a way to obtain clusters passivated with nitrogen according to [11]. Another way to passivate the Fe clusters is to proceed via the overall dissociation process using massive exposure. This approach is described in the next section. Note that we did not investigate the non-dissociative adsorption of nitrogen in the temperature range 200-400 K, which is the temperature range of interest according to [11], after the cluster passivation by slow $^{15}\text{N}_2$ dissociation. We recommend to do it in future investigations.

6.3.2 Passivation of Fe clusters by massive exposure

The next TDS investigations are performed in order to verify if nitrogen molecules are able to adsorb without dissociation on passivated Fe clusters in accordance with the DFT calculations that inspired our experiments [11]. In order to fully saturate the Fe clusters

6.3. Nitrogen desorption from Fe clusters on graphene/Ir(111)

with dissociated N_2 , we expose them to 10^{-4} mbar N_2 for 30 min (10^6 L of N_2) at 300 K. This procedure is motivated by the very small sticking coefficient for the dissociative adsorption of molecular nitrogen on single crystal Fe surfaces [2, 89, 90], and assuming similar behavior for our Fe clusters adsorbed on graphene/Ir(111).

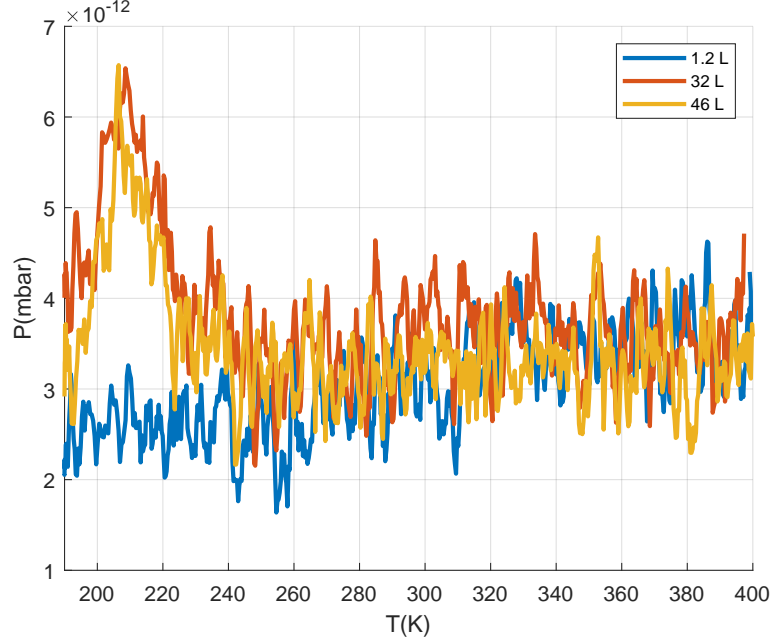


Figure 6.6 – TDS of $^{15}\text{N}_2$ from Fe clusters on graphene/Ir(111). Ramp speed: 1 K/s.

This relatively large exposure increases the background pressure in the UHV chamber and takes about 120 min to be pumped down into the low 10^{-10} mbar again. After this, the TDS are performed according to the same procedure as described in the previous section. The sample is exposed to $^{15}\text{N}_2$, this time at a temperature of $T_{\text{exp}} = 190$ K. TDS are realized between 190 K and 400 K with a temperature ramp of 1 K/s. This temperature range corresponds to the binding energy calculated in [11] for N_2 attachment on the nitrogenated cluster (in the calculations the clusters are placed on $\text{MgO}(100)$).

As seen from inspection of figure 6.6, no significant desorption peaks are visible in the temperature range studied. A peak above 200 K is present for the two highest exposures. Considering the small amplitude of this peak, below 10^{-11} mbar, compared to the other peak heights reported above that are 2-3 orders of magnitude more intense, it seems unlikely that it corresponds to the desorption $^{15}\text{N}_2$ from the clusters we are looking for. Therefore, we attribute it to a parasitic signal due to the prior exposure.

In conclusion, our attempt to demonstrate molecular N_2 adsorption on N-passivated Fe clusters did not yield the desired result, it rather shows that Fe clusters on graphene/Ir(111) of the investigated size are poisoned by the dissociated N_2 . Several reasons can explain this result. First of all, the calculations are performed for Fe_7 on MgO , and not on

supported graphene. Second, the clusters on which the TDS are performed are much larger than the desired cluster size, $\bar{n}_1 = 35$ with 0.4 ML Fe, while the DFT calculations consider a cluster of 7 atoms. Reducing the amount of Fe deposited yields smaller clusters. However, these clusters diffuse in the temperature range where the above reported desorption peaks are located, and in particular at the temperature where the desorption of the chemisorbed molecular species is expected. The growth of thermally stable Fe clusters with a size of about 7 atoms per cluster should be a priority to consider in future research efforts. We suggest to fix the clusters by deposition of a small amount of a high cohesive energy metal on the template [85]. For this purpose, rhodium should be a good candidate as an efficient seeding material [91]. Another unknown in the experiment is the effect of exposure of 10^6 L of N_2 on the sample in order to passivate the clusters. With a gas impurity level of 10^{-6} , the dose of gas contaminants is of the order of 10 L which could change the catalytic activity of the Fe clusters.

7 Conclusion

A highly sensitive gas detector (sniffer) has been developed and integrated into a UHV system in order to study the catalytic properties of surface-supported metal clusters. The experimental setup enables for in-situ STM measurements to characterize the atomic scale morphology of the clusters allowing us to establish a link between cluster morphology and catalytic properties.

The sniffer was successfully tested by thermal desorption spectroscopy of Xe adsorbed on a Ag(100) surface. The spectra showed zero order desorption and demonstrated the very high sensitivity of the sniffer of 10^{-6} monolayers. An exchange process between Fe adatoms and Ag surface atoms was detected by N₂ desorption spectra. The presence of Fe adatoms on the Ag(100) surface changes significantly the desorption spectrum of N₂ adsorbed at the surface. The effect of the Fe adatoms decreases after annealing at 120 K, and disappears completely after annealing at 140 K, which we interpret as the result of the exchange process mentioned above. This result is in agreement with the onset of Fe/Ag(100) exchange reported by low-energy ion scattering at 130 K. It demonstrates the ability of the sniffer to detect surface processes that modify the surface morphology and its adsorption-desorption properties.

In order to study a system related to the one considered in the DFT calculations that motivate our project, we investigated the growth of Fe clusters on MgO thin films on Ag(100). The Fe clusters were obtained by thermal ripening: 0.05 to 0.07 ML of Fe was deposited on 1 ML MgO at 50 K followed by annealing at 300 K. The cluster size was approximately 12 atoms per cluster. No N₂ desorption peak was observed after exposure to molecular nitrogen. This desorption experiment was performed on unpassivated Fe clusters. An idea for future measurements is to revisit the desorption experiment with Fe clusters passivated via the slow N₂ dissociation approach described in chapter 6.

Using the moiré pattern formed by graphene on Ir(111) as template to control the Fe cluster growth was successful. The Fe clusters present a long range order with the same periodicity than the moiré pattern. Most of the primary clusters formed during

Chapter 7. Conclusion

the Fe deposition at 50 K remain stable after annealing at 400 K. Coarsening of the clusters proceeds via Smoluchowski ripening when annealing at higher temperatures. TDS investigations revealed the existence of multiple adsorption sites of N_2 on these Fe clusters.

Two approaches were tested for the passivation of the Fe clusters by chemisorbed N atoms. The first consists in the slow dissociation of N_2 adsorbed on the clusters. Evidence of the N_2 dissociation was observed by TDS: after the cluster passivation, one of the previously observed desorption peaks is largely depleted, demonstrating that the corresponding adsorption site is occupied by strongly bound atomic nitrogen. In the second approach we use massive N_2 exposure at room temperature to overcome the very low sticking coefficient of dissociative adsorption of nitrogen on iron. In this case no evidence of passivation was observed, and no desorption peak of molecularly adsorbed N_2 was obtained in the temperature range of interest (200-400 K). Because of the multiple uncontrolled parameters implied by the second approach, such as contamination of the clusters by unwanted molecules, and modification of the surface morphology induced by the massive exposure, we do not recommend this procedure in future experiments.

The experimental device combining variable temperature STM and sniffer was shown to be operational to investigate adsorption/desorption processes and reactions on particles self-assembled at surfaces. A promising system to be investigated in the future could be Fe clusters on graphene/Ir(111) pinned by a small amount of seeding material such as Ir or Rh. In this way, the thermal cluster stability could be maintained even for smaller Fe clusters.

A Fe flux calibration on Ir(111)

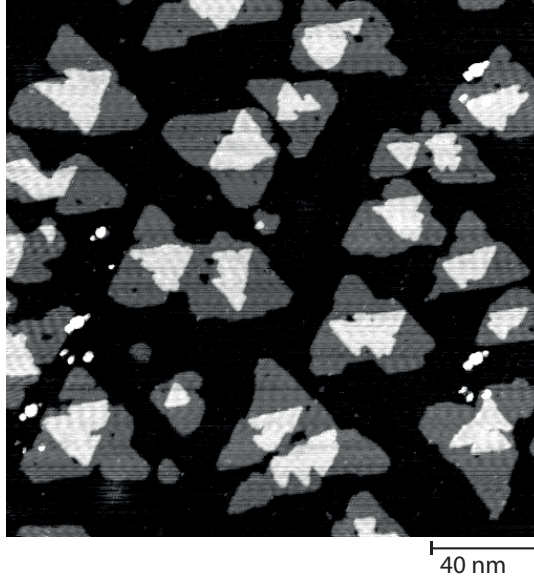


Figure A.1 – STM image of Fe deposited on Ir(111) at 300 K, $I = 1$ nA, $V = 0.2$ V. The Fe coverage is determined to be $\theta = 0.53 \pm 0.02$ ML.

The Fe flux, obtained by the evaporation of an Fe rod by electron bombardment, is calibrated by STM investigation of Fe islands grown on Ir(111). The Ir(111) sample, prepared with repeated cycles of Ar^+ sputtering (1500 eV, $3.1 \mu\text{A}/\text{cm}^2$, 300 K) and annealing at 1450 K for 1 min, is exposed to the reference Fe flux for 200 s. The morphology of the obtained Fe islands is visible in figure A.1. The growth is of the Stranski-Krastanov type, with the clean substrate exposed, as well as Fe covered regions that are one and two monolayers thick. The coverage determination is performed by evaluating the surface portion covered by one and two layers of Fe. Assuming that the Fe islands are pseudomorphic, we obtain an average coverage of $\theta = 0.53 \pm 0.02$ ML, where 1 ML corresponds to the surface atomic density of Ir(111). The deduced Fe flux is 0.15 ± 0.006 ML/min.

Bibliography

- [1] G. Ertl, P. R. Norton, and J. Rüstig. *Kinetic Oscillations in the Platinum-Catalyzed Oxidation of Co*. Phys. Rev. Lett. **49**, 177–180 (1982).
- [2] G. Ertl, S. B. Lee, and M. Weiss. *Kinetics of nitrogen adsorption on Fe(111)*. Surf. Sci. **114**, 515–526 (1982).
- [3] J. Libuda and H.-J. Freund. *Molecular beam experiments on model catalysts*. Surf. Sci. Rep. **57**, 157–298 (2005).
- [4] J. Kästner and P. E. Blöchl. *Ammonia Production at the FeMo Cofactor of Nitrogenase: Results from Density Functional Theory*. J. Am. Chem. Soc. **129**, 2998–3006 (2007).
- [5] J. Kim and D. C. Rees. *Nitrogenase and biological nitrogen fixation*. J. Am. Chem. Soc. **33**, 389–397 (1994).
- [6] B. K. Burgess and D. J. Lowe. *Mechanism of Molybdenum Nitrogenase*. Chem. Rev. **96**, 2983–3012 (1996).
- [7] B. Hinnemann and J. K. Nørskov. *Modeling a Central Ligand in the Nitrogenase FeMo Cofactor*. J. Am. Chem. Soc. **125**, 1466–1467 (2003).
- [8] T. H. Rod, A. Logadottir, and J. K. Nørskov. *Ammonia synthesis at low temperatures*. J. Chem. Phys. **112**, 5343 (2000).
- [9] Ž. Šljivančanin and A. Pasquarello. *Nitrogen adsorption on a supported iron nanocluster*. Vacuum **74**, 173–177 (2004).
- [10] Ž. Šljivančanin and A. Pasquarello. *Supported nanoclusters: Preadsorbates tuning catalytic activity*. Phys. Rev. B **71**, 081403–081403 (2005).
- [11] Ž. Šljivančanin, H. Brune, and A. Pasquarello. *Nitrogen fixation at passivated Fe nanoclusters supported by an oxide surface: Identification of viable reaction routes using density functional calculations*. Phys. Rev. B **80**, 075407 (2009).
- [12] H. Brune. *Microscopic view of epitaxial metal growth: nucleation and aggregation*. Surf. Sci. Rep. **31**, 125–229 (1998).

Bibliography

- [13] S. Bonanni, K. Aït-Mansour, M. Hugentobler, H. Brune, and W. Harbich. *An experimental setup combining a highly sensitive detector for reaction products with a mass-selected cluster source and a low-temperature STM for advanced nanocatalysis measurements*. Eur. Phys. J. D **63**, 241–249 (2011).
- [14] S. Bonanni. *Cluster-surface interaction and catalytic activity*. Ph.D. thesis, EPFL, Lausanne (2012).
- [15] H. Achour. *Transition metal clusters on h-BN/Rh(111)*. Ph.D. thesis, EPFL, Lausanne (2017).
- [16] H. Röder. *Microscopic processes in heteroepitaxial growth: nucleation, growth and alloying of silver on the (111) surface of platinum*. Ph.D. thesis, EPFL, Lausanne (1994).
- [17] H. Brune, H. Röder, K. Bromann, and K. Kern. *Kinetic processes in metal epitaxy studied with variable temperature STM: Ag/Pt(111)*. Thin Solid Films **264**, 230–235 (1995).
- [18] K. Bromann. *Controlling epitaxial morphologies on the microscopic scale*. Ph.D. thesis, EPFL, Lausanne (1997).
- [19] M. Giovannini. *Metallic thin layers and nanostructures: fabrication and characterization*. Ph.D. thesis, EPFL, Lausanne (2000).
- [20] S. Vlaic. *Magnetism and atomic scale structure of bimetallic nanostructures at surfaces*. Ph.D. thesis, EPFL, Lausanne (2013).
- [21] B. Voigtländer. *Technical Aspects of Scanning Probe Microscopy*. In *Scanning probe microscopy: atomic force microscopy and scanning tunneling microscopy*, pp.31–63. Springer Berlin Heidelberg, Berlin (2015).
- [22] G. Binnig, H. Rohrer, C. Gerber, and E. Weibel. *Tunneling through a controllable vacuum gap*. Appl. Phys. Lett. **40**, 178–180 (1982).
- [23] G. Binnig and H. Rohrer. *Scanning tunneling microscopy*. Surf. Sci. **126**, 236–244 (1983).
- [24] R. Young, J. Ward, and F. Scire. *The topografiner: an instrument for measuring surface microtopography*. Rev. Sci. Instrum. **43**, 999–1011 (1972).
- [25] F. D. Natterer, K. Yang, W. Paul, P. Willke, T. Choi, T. Greber, A. J. Heinrich, and C. P. Lutz. *Reading and writing single-atom magnets*. Nature **543**, 226–228 (2017).
- [26] C. Chen. *Introduction to scanning tunneling microscopy*. Oxford University Press (2008).

-
- [27] N. Weiss. *Propriétés magnétiques de nanostructures de cobalt adsorbées*. Ph.D. thesis, EPFL, Lausanne (2004).
- [28] P. Feulner and D. Menzel. *Simple ways to improve "flash desorption" measurements from single crystal surfaces*. J. Vac. Sci. Technol. **17**, 662–663 (1980).
- [29] P. A. Redhead. *Thermal desorption of gases*. Vacuum **12**, 203–211 (1962).
- [30] J. E. Campana. *Elementary theory of the quadrupole mass filter*. Int. J. Mass Spectrom. Ion Phys. **33**, 101–117 (1980).
- [31] D. Gerlich. *Inhomogeneous RF fields: a versatile tool for the study of processes with slow ions*, pp.1–176. John Wiley & Sons, Ltd (2007).
- [32] S. Wright, S. O'Prey, R. Syms, H. Guodong, and A. Holmes. *Microfabricated quadrupole mass spectrometer with a brubaker prefilter*. J. Microelectromech. Syst. **19**, 325–337 (2010).
- [33] C. R. Henry, C. Chapon, and C. Duriez. *Precursor state in the chemisorption of CO on supported palladium clusters*. J. Chem. Phys. **95**, 700–705 (1991).
- [34] K. Judai, S. Abbet, A. S. Wörz, M. A. Röttgen, and U. Heiz. *Turn-over frequencies of catalytic reactions on nanocatalysts measured by pulsed molecular beams and quantitative mass spectrometry*. Int. J. Mass Spectrom. **229**, 99–106 (2003).
- [35] C. J. Harding, S. Kunz, V. Habibpour, V. Teslenko, M. Arenz, and U. Heiz. *Dual pulsed-beam controlled mole fraction studies of the catalytic oxidation of CO on supported Pd nanocatalysts*. J. Catal. **255**, 234–240 (2008).
- [36] R. J. Behm, C. R. Brundle, and K. Wandelt. *The underlayer influence on photoemission and thermal desorption of xenon adsorbed on Ag(111)*. J. Chem. Phys. **85**, 1061–1073 (1986).
- [37] H. Schlichting and D. Menzel. *High resolution, wide range, thermal desorption spectrometry of rare gas layers: sticking, desorption kinetics, layer growth, phase transitions, and exchange processes*. Surf. Sci. **272**, 27–33 (1992).
- [38] W. Widdra, S. Payne, and H. Kreuzer. *Rare-gas thermal desorption from flat and stepped platinum surfaces: Lateral interactions and the influence of dimensionality*. Phys. Rev. B **57**, 4111–4126 (1998).
- [39] R. S. Smith, R. A. May, and B. D. Kay. *Desorption Kinetics of Ar, Kr, Xe, N₂, O₂, CO, methane, ethane, and propane from graphene and amorphous solid water surfaces*. J. Phys. Chem. B **120**, 1979–1987 (2016).
- [40] A. Ouvrard, J. Niebauer, A. Ghalgaoui, C. Barth, C. R. Henry, and B. Bourguignon. *Characterization of thin MgO films on Ag(001) by low-energy electron diffraction and scanning tunneling microscopy*. J. Phys. Chem. C **115**, 8034–8041 (2011).

Bibliography

- [41] J. Pal, M. Smerieri, E. Celasco, L. Savio, L. Vattuone, and M. Rocca. *Morphology of monolayer MgO Films on Ag(100): switching from corrugated islands to extended flat terraces*. Phys. Rev. Lett. **112**, 126102 (2014).
- [42] J. D. Wrigley and G. Ehrlich. *Surface diffusion by an atomic exchange mechanism*. Phys. Rev. Lett. **44**, 661–663 (1980).
- [43] G. L. Kellogg. *Direct observations of adatom–surface-atom replacement: Pt on Ni(110)*. Phys. Rev. Lett. **67**, 216–219 (1991).
- [44] C. Massobrio, F. Patthey, H.-V. Roy, and W. D. Schneider. *Heterodeposition on metallic surfaces: Structure and energetics in the Pd/Ag(110) and Pt/Ag(110) systems*. Phys. Rev. B **52**, 2063–2065 (1995).
- [45] F. Patthey, C. Massobrio, and W.-D. Schneider. *Dynamics of surface alloying: Determination of diffusion barriers from photoelectron spectra*. Phys. Rev. B **53**, 13146–13149 (1996).
- [46] R. Belkhou, R. Flammini, M. Marsi, A. Taleb-Ibrahimi, L. Gregoratti, A. Barinov, and M. Kiskinova. *Role of gold segregation in the growth mode and the morphology of Fe/Au(001) magnetic thin films*. Surf. Sci. **532-535**, 63–69 (2003).
- [47] O. S. Hernán, A. L. Vázquez de Parga, J. M. Gallego, and R. Miranda. *Self-surfactant effect on Fe/Au(100): place exchange plus Au self-diffusion*. Surf. Sci. **415**, 106–121 (1998).
- [48] E. Lundgren, B. Stanka, G. Leonardelli, M. Schmid, and P. Varga. *Interlayer diffusion of adatoms: a scanning-tunneling microscopy study*. Phys. Rev. Lett. **82**, 5068–5071 (1999).
- [49] M. H. Langelaar and D. O. Boerma. *Fe adatoms on Ag(100): site exchange and mobility*. Surf. Sci. **395**, 131–137 (1998).
- [50] L. Vitos, A. V. Ruban, H. L. Skriver, and J. Kollár. *The surface energy of metals*. Surf. Sci. **411**, 186–202 (1998).
- [51] H. R. Siddiqui, P. J. Chen, X. Guo, and J. T. Yates. *A comparative kinetic study of xenon adsorption on a flat Pt(111) and stepped Pt(557) and Pt(112) surfaces*. J. Chem. Phys. **92**, 7690–7699 (1990).
- [52] F. D. Natterer, F. Patthey, and H. Brune. *Quantifying residual hydrogen adsorption in low-temperature STMs*. Surf. Sci. **615**, 80–87 (2013).
- [53] Q. Dubout, F. Donati, C. Wäckerlin, F. Calleja, M. Etzkorn, A. Lehnert, L. Claude, P. Gambardella, and H. Brune. *Controlling the spin of Co atoms on Pt(111) by hydrogen adsorption*. Phys. Rev. Lett. **114**, 106807 (2015).

-
- [54] F. Donati, Q. Dubout, G. Autès, F. Patthey, F. Calleja, P. Gambardella, O. Yazyev, and H. Brune. *Magnetic moment and anisotropy of individual Co atoms on graphene*. Phys. Rev. Lett. **111**, 236801 (2013).
- [55] H. R. Sadeghi and V. E. Henrich. *Rh on TiO₂: Model catalyst studies of the strong metal-support interaction*. Appl. Surf. Sci. **19**, 330–340 (1984).
- [56] C. Xu, W.-S. Oh, D. Y. Kim, and D. Goodman. *Characterization of metal clusters (Pd and Au) supported on various metal oxide surfaces (MgO and TiO₂)*. J. Vac. Sci. Technol. **15**, 1261–1268 (1997).
- [57] A. Kolmakov and D. W. Goodman. *Scanning tunneling microscopy of gold clusters on TiO₂(110): CO oxidation at elevated pressures*. Surf. Sci. **490**, L597–L601 (2001).
- [58] G. Prevot, O. Meerson, L. Piccolo, and C. Henry. *Reactivity of supported metal clusters: The reduction of NO by CO on a Pd/MgO catalyst*. J. Phys. Condens. Matter **14**, 4251–4269 (2002).
- [59] D. A. Bulushev, L. Kiwi-Minsker, I. Yuranov, E. I. Suvorova, P. A. Buffat, and A. Renken. *Structured Au/FeO_x/C catalysts for low-temperature CO oxidation*. J. Catal. **210**, 149–159 (2002).
- [60] A. Vijay, G. Mills, and H. Metiu. *Adsorption of gold on stoichiometric and reduced rutile TiO₂(110) surfaces*. J. Chem. Phys. **118**, 6536–6551 (2003).
- [61] A. F. Carlsson, M. Naschitzki, M. Bäumer, and H.-J. Freund. *The structure and reactivity of Al₂O₃-supported cobalt-palladium particles: a CO-TPD, STM, and XPS study*. J. Phys. Chem. B **107**, 778–785 (2003).
- [62] M. Bowker, P. Stone, P. Morrall, R. Smith, R. Bennett, N. Perkins, R. Kvon, C. Pang, E. Fourre, and M. Hall. *Model catalyst studies of the strong metal-support interaction: Surface structure identified by STM on Pd nanoparticles on TiO₂(110)*. J. Catal. **234**, 172–181 (2005).
- [63] T. P. St.Clair and D. W. Goodman. *Metal nanoclusters supported on metal oxide thin films: bridging the materials gap*. Top. Catal. **13**, 5–19 (2000).
- [64] Z. Ding, L. Yan, Z. Li, W. Ma, G. Lu, and S. Meng. *Controlling catalytic activity of gold cluster on MgO thin film for water splitting*. Phys. Rev. Mater. **1**, 045404 (2017).
- [65] S. Abbet, U. Heiz, A. Maria Ferrari, L. Giordano, C. Di Valentin, and G. Pacchioni. *Nano-assembled Pd catalysts on MgO thin films*. Thin Solid Films **400**, 37–42 (2001).
- [66] H.-J. Freund. *Model studies in heterogeneous catalysis*. Chem. Eur. J. **16**, 9384–9397 (2010).

Bibliography

- [67] H.-J. Freund, M. Heyde, H. Kuhlenbeck, N. Nilius, T. Risse, T. Schmidt, S. Shaikhutdinov, and M. Sterrer. *Chapter model systems in heterogeneous catalysis at the atomic level: a personal view*. Sci. China Chem. **63**, 426–447 (2020).
- [68] H. Brune. *Epitaxial growth of thin films*, chap. 20, pp.421–492. Wiley-VCH Verlag GmbH & Co. KGaA (2013).
- [69] G. Haas, A. Menck, H. Brune, J. V. Barth, J. A. Venables, and K. Kern. *Nucleation and growth of supported clusters at defect sites: Pd/MgO(001)*. Phys. Rev. B **61**, 11105–11108 (2000).
- [70] W. T. Wallace, B. K. Min, and D. W. Goodman. *The stabilization of supported gold clusters by surface defects*. J. Mol. Catal. A: Chem. **228**, 3–10 (2005).
- [71] H.-J. Shin, J. Jung, K. Motobayashi, S. Yanagisawa, Y. Morikawa, Y. Kim, and M. Kawai. *State-selective dissociation of a single water molecule on an ultrathin MgO film*. Nat. Mater. **9**, 442–447 (2010).
- [72] S. Baumann, I. G. Rau, S. Loth, C. P. Lutz, and A. J. Heinrich. *Measuring the three-dimensional structure of ultrathin insulating films at the atomic scale*. ACS Nano **8**, 1739–1744 (2014).
- [73] G. Binnig, K. H. Frank, H. Fuchs, N. Garcia, B. Reihl, H. Rohrer, F. Salvan, and A. R. Williams. *Tunneling spectroscopy and inverse photoemission: image and field states*. Phys. Rev. Lett. **55**, 991–994 (1985).
- [74] E. Fernandes, F. Donati, F. Patthey, S. Stavrić, Ž. Šljivančanin, and H. Brune. *Adsorption sites of individual metal atoms on ultrathin MgO(100) films*. Phys. Rev. B **96**, 045419 (2017).
- [75] J. Pal, M. Smerieri, E. Celasco, L. Savio, L. Vattuone, R. Ferrando, S. Tosoni, L. Giordano, G. Pacchioni, and M. Rocca. *How growing conditions and interfacial oxygen affect the final morphology of MgO/Ag(100) films*. J. Phys. Chem. C **118**, 26091–26102 (2014).
- [76] I. Dézsi, C. Fetzter, I. Szűcs, B. Degroote, A. Vantomme, T. Kobayashi, and A. Nakanishi. *Ultrathin Fe layers on Ag (100) surface*. Surf. Sci. **601**, 2525–2531 (2007).
- [77] M. Canepa, M. Salvietti, A. Campora, and L. Mattera. *Interdiffusion and segregation in the growth of thin Fe films on Ag(100): an ARUPS-MDS study*. J. Electron Spectrosc. Relat. Phenom. **76**, 471–476 (1995).
- [78] T. Wiederholt, H. Brune, J. Wintterlin, R. Behm, and G. Ertl. *Formation of two-dimensional sulfide phases on Al(111): an STM study*. Surf. Sci. **324**, 91 – 105 (1995).

-
- [79] A. Lehnert, A. Krupski, S. Degen, K. Franke, R. Decker, S. Rusponi, M. Kralj, C. Becker, H. Brune, and K. Wandelt. *Nucleation of ordered Fe islands on $Al_2O_3/Ni_3Al(111)$* . Surf. Sci. **600**, 1804 – 1808 (2006).
- [80] M. Schmid, G. Kresse, A. Buchsbaum, E. Napetschnig, S. Gritschneider, M. Reichling, and P. Varga. *Nanotemplate with holes: ultrathin alumina on $Ni_3Al(111)$* . Phys. Rev. Lett. **99** (2007).
- [81] A. T. N'Diaye, S. Bleikamp, P. J. Feibelman, and T. Michely. *Two-dimensional Ir cluster lattice on a graphene moiré on $Ir(111)$* . Phys. Rev. Lett. **97**, 215501 (2006).
- [82] S. Marchini, S. Günther, and J. Wintterlin. *Scanning tunneling microscopy of graphene on $Ru(0001)$* . Phys. Rev. B **76**, 075429 (2007).
- [83] C. Berger, Z. Song, X. Li, X. Wu, N. Brown, C. Naud, D. Mayou, T. Li, J. Hass, A. N. Marchenkov, E. H. Conrad, P. N. First, and W. A. de Heer. *Electronic confinement and coherence in patterned epitaxial graphene*. Science **312**, 1191 (2006).
- [84] A. N'Diaye, J. Coraux, T. Plasa, C. Busse, and T. Michely. *Structure of epitaxial graphene on $Ir(111)$* . New J. Phys. **10**, 043033 (2008).
- [85] A. T. N'Diaye, T. Gerber, C. Busse, J. Mysliveček, J. Coraux, and T. Michely. *A versatile fabrication method for cluster superlattices*. New J. Phys. **11**, 103045 (2009).
- [86] F. Natterer, F. Patthey, and H. Brune. *Ring state for single transition metal atoms on boron nitride on $Rh(111)$* . Phys. Rev. Lett. **109**, 066101 (2012).
- [87] W. Auwärter, M. Muntwiler, T. Greber, and J. Osterwalder. *Co on $h\text{-BN}/Ni(111)$: from island to island-chain formation and Co intercalation*. Surf. Sci. **511**, 379–386 (2002).
- [88] T. Gerber, J. Knudsen, P. J. Feibelman, E. Grånäs, P. Stratmann, K. Schulte, J. N. Andersen, and T. Michely. *CO-induced smoluchowski ripening of Pt cluster arrays on the graphene/ $Ir(111)$ moiré*. ACS Nano **7**, 2020–2031 (2013).
- [89] F. Bozso, G. Ertl, M. Grunze, and M. Weiss. *Interaction of nitrogen with iron surfaces: I. $Fe(100)$ and $Fe(111)$* . J. Catal. **49**, 18–41 (1977).
- [90] F. Bozso, G. Ertl, and M. Weiss. *Interaction of nitrogen with iron surfaces: II. $Fe(110)$* . J. Catal. **50**, 519–529 (1977).
- [91] D. Mousadakos. *Rare Earth and bimetallic transition metal islands at surfaces*. Ph.D. thesis, EPFL, Lausanne (2017).

Remerciements

La réalisation de ce travail de thèse a été une longue aventure humaine, intellectuelle et technique que je n'ai pas menée seul. Je tiens donc à remercier toutes les personnes impliquées dans ce projet dont le soutien a été essentiel.

Tout d'abord, je remercie le professeur Harald Brune, qui m'a donné l'opportunité de travailler dans son groupe de recherche pour réaliser cette thèse. J'adresse également mes plus grands remerciements à Marina Pivetta pour avoir supervisé mon travail. Ses conseils et son aide lors de la rédaction ont été essentielles. Je remercie aussi le comité d'experts, Marco Grioni, Renald Schaub et Christian Wäckerlin, pour leur travail de critique scientifique de cette thèse, ainsi que le président du jury, Frédéric Courbin, pour l'organisation de l'examen. Le sniffer, qui occupe une place centrale dans ce projet, est un instrument de mesure initialement imaginé par Wolfgang Harbich. Je tiens à le remercier pour tous ses conseils et sa disponibilité. Pendant toutes ses années nous avons aussi collaboré dans le cadre de l'enseignement duquel je garde un très bon souvenir. La manipulation d'une expérience aussi complexe qu'une chambre à vide et tous les outils associés requièrent un savoir-faire pointu. François Patthey et Stefano Rusponi m'ont fait bénéficier de leur grande expérience dans le domaine, spécialement en ce qui concerne le STM. J'ai aussi pensé pour Stephan Fedrigo, disparu en 2020, avec qui j'ai eu de nombreuses discussions passionnantes. Je remercie également Claude Amendola et Gilles Grandjean pour tout le soutien technique qu'ils m'ont donné et qui a permis de mener les différentes expériences à bien. Une partie significative des résultats sur MgO/Ag(100) ont été obtenues pendant ma collaboration avec Edgar Fernandes à qui j'adresse mes plus grands remerciements pour son aide. Merci enfin à toutes les personnes qui m'ont accompagné et soutenu pendant ces années de doctorat. Ma famille, mes amis, ainsi que tous les collaborateurs du LNS.

Lausanne, le 25 Mars 2021

Jean-Guillaume de Groot.

Jean-Guillaume de Groot

Curriculum Vitae

Education

- 2015–2021 **Ecole Polytechnique Fédéral de Lausanne**, *PhD in Physics*.
- 2013–2015 **Ecole Polytechnique Fédéral de Lausanne**, *Master in Physics*.
- 2008–2012 **Ecole Polytechnique Fédéral de Lausanne**, *Bachelor in Physics*.
- 2008 **Baccalauréat Scientifique**, Lycée Lapérouse, Albi (France).

Work experience

- 2014 **ETEL S.A**, *4 months internship in the Advanced Research & Development Department*.
Investigation and physical explanation of the electrical motors behavior of in specified conditions. The work consisted in combining a **theoretical model**, **numerical simulations** and **experimental data** to characterize the behavior of the motors. The final report written during this work had been appreciate by the different R&D departments and by the company founder.
- 2013 **Ecole Polytechnique Fédéral de Lausanne**, *Laboratory assistant*.
Measuring mechanic and magnetic perturbations in a room for the installation of a high resolution electron microscope.
- 2011–2015 **Ecole Polytechnique Fédéral de Lausanne**, *Student assistant*, EPFL.
Support for student groups to resolve physics exercises.

Other activities

- Music **Cello**, "*Certificat de Fin d'Etudes Musicales*", Albi music school, 2008.
 - Member of the "Orchestre Symphonique Universitaire de Lausanne"

Personal details

- Birth year 1990
- Nationalities Swiss, French, Dutch
- Email jeanguillaume.degroot@gmail.com